# Global invariant manifolds near a Shilnikov homoclinic bifurcation

Pablo Aguirre [a1], Bernd Krauskopf [b] and Hinke M. Osinga [b]

November 2011

[a] Department of Engineering Mathematics, University of Bristol
Bristol BS8 1TR, United Kingdom

[b] Department of Mathematics, The University of Auckland
Private Bag 92019, Auckland 1142, New Zealand

**Abstract**

We consider a three-dimensional vector field with a Shilnikov homoclinic orbit that converges to a saddle-focus equilibrium in both forward and backward time. The one-parameter unfolding of this gloal bifurcation depends on the sign of the saddle quantity. When it is negative, breaking the homoclinic orbit produces a single stable periodic orbit; this is known as the simple Shilnikov bifurcation. However, when the saddle quantity is positive, the mere existence of a Shilnikov homoclinic orbit induces complicated dynamics, and one speaks of the chaotic Shilnikov bifurcation; in particular, one finds suspended horseshoes and countably many periodic orbits of saddle type. These well-known and celebrated results on the Shilnikov homoclinic bifurcation have been obtained by the classical approach of reducing a Poincaré return map to a one-dimensional map.

In this paper, we study the implications of the transition through a Shilnikov bifurcation for the overall organisation of the three-dimensional phase space of the vector field. To this end, we focus on the role of the two-dimensional global stable manifold of the equilibrium, as well as those of bifurcating saddle periodic orbits. We compute the respective two-dimensional global manifolds, and their intersection curves with a suitable sphere, as families of orbit segments with a two-point boundary-value-problem setup. This allows us to determine how the arrangement of global manifolds changes through the bifurcation and how this influences the topological organisation of phase space. For the simple Shilnikov bifurcation, we show how the stable manifold of the saddle focus forms the basin boundary of the bifurcating stable periodic orbit. For the chaotic Shilnikov bifurcation, we find that the stable manifold of the equilibrium is an accessible set of the stable manifold of a chaotic saddle that contains countably many periodic orbits of saddle type. In intersection with a suitably chosen sphere we find that this stable manifold is an indecomposable continuum consisiting of infinitely many closed curves that are locally a Cantor bundle of arcs.

[1]Supported by a CONICYT grant and an ORS award.

# 1 Introduction

The problem of describing the organization of phase space of a dynamical system, given by the flow of a vector field or the iteration of a map, has been the subject of innumerable studies. With many examples arising from real-world phenomena, the desire to understand the underlying behavior of vector fields and maps in such applications has led to a healthy symbiosis between theoretical and practical aspects of the subject; see, for example, [4, 27, 39, 40, 44, 62] as entry points into the extensive literature.

We consider here dynamics with continuous time, described by a vector field. For this type of dynamical system the analysis of local phenomena is well understood via normal forms and desingularization techniques [27, 40, 62]. However, the study of global features of the dynamics remains much more challenging. Homoclinic and heteroclinic connections, between saddle equilibria and/or periodic orbits, are examples of global bifurcations arising in many applied systems [2, 28, 44, 49, 57, 58]. A small perturbation of a system parameter typically breaks such connections, and their presence can have a dramatic effect on the overall dynamics — creating (or destroying) basins of attraction and, generally, changing the topology of phase space. A particular case is a homoclinic orbit of Shilnikov type that approaches a saddle-focus equilibrium in a spiraling fashion. Perhaps the most celebrated and intriguing feature of a Shilnikov homoclinic bifurcation is the fact that it constitutes the simplest global phenomenon that can induce chaotic dynamics, known as Shilnikov chaos [40, 52, 53, 54, 62]. The Shilnikov homoclinic bifurcation occurs already in vector fields of dimension three — the lowest possible phase-space dimension — and it is of codimension one, meaning that it is unfolded by a single parameter.

## 1.1 Mathematical setting

The Shilnikov homoclinic bifurcation is our main object of study and, hence, we consider a vector field of the form

$$\dot{x} = f(\mathbf{x}, \eta), \tag{1}$$

where $\mathbf{x} \in \mathbb{R}^3$, $\eta \in \mathbb{R}$ is a parameter, and $f : \mathbb{R}^3 \times \mathbb{R} \to \mathbb{R}^3$ is sufficiently smooth. The vector field (1) induces a flow $\varphi^t$ on $\mathbb{R}^3$ that determines the dynamics. We assume that there is a hyperbolic saddle-focus equilibrium $p = (p_x, p_y, p_z)$; more precisely, the Jacobian matrix $Df(p)$ has one unstable real eigenvalue $\lambda^u > 0$ and a pair of stable complex conjugate eigenvalues $\lambda^s_{1,2}$ with $Re(\lambda^s_{1,2}) < 0$ (the other case of a hyperbolic saddle-focus equilibrium can be obtained simply by reversing time). We denote the associated stable and unstable linear eigenspaces by $E^s(p)$ and $E^u(p)$, respectively.

The local stable and unstable manifolds of $p$ are then defined by

$$\begin{aligned} W^s_{\text{loc}}(p) &= \left\{\mathbf{x} \in U \mid \varphi^t(\mathbf{x}) \to p \text{ as } t \to \infty\,, \text{ and } \varphi^t(\mathbf{x}) \in U \ \forall t \geq 0\right\}, \\ W^u_{\text{loc}}(p) &= \left\{\mathbf{x} \in U \mid \varphi^t(\mathbf{x}) \to p \text{ as } t \to -\infty, \text{ and } \varphi^t(\mathbf{x}) \in U \ \forall t \leq 0\right\}, \end{aligned}$$

where $U \subset \mathbb{R}^3$ is a neighborhood of $p$. Their respective extensions to the rest of the phase space are the global (un)stable manifolds defined by

$$\begin{aligned} W^s(p) &= \left\{\mathbf{x} \in \mathbb{R}^3 \mid \varphi^t(\mathbf{x}) \to p \text{ as } t \to \infty\right\}, \\ W^u(p) &= \left\{\mathbf{x} \in \mathbb{R}^3 \mid \varphi^t(\mathbf{x}) \to p \text{ as } t \to -\infty\right\}. \end{aligned}$$

According to the Stable Manifold Theorem [27, 40, 62], the sets $W^s(p)$ and $W^u(p)$ are, respectively, two-dimensional and one-dimensional (immersed) manifolds that are as smooth as $f$ and tangent at $p$ to $E^s(p)$ and $E^u(p)$.

The vector field $f$ can also have attracting equilibria and periodic orbits. Any such attracting invariant object, say $A$, has a neighborhood $U$ that satisfies

$$\varphi^t(U) \subset U \quad \forall t \geq 0 \quad \text{and} \quad \bigcap_{t>0} \varphi^t(U) = A. \tag{2}$$

The basin of attraction $\mathcal{B}(A)$ of $A$ is the set of points in phase space that converge to it, that is,

$$\mathcal{B}(A) = \bigcup_{t\leq 0} \varphi^t(U),$$

where $U \subset \mathbb{R}^3$ is any open neighborhood of $A$ satisfying (2).

### 1.2 The two cases of the Shilnikov bifurcation

Suppose that there is a homoclinic orbit $\Gamma_0$ of (1) for $\eta = \eta^*$, which connects the equilibrium $p$ back to itself. Geometrically, the connecting orbit is formed by one branch of the unstable manifold $W^u(p)$, which lies entirely in the surface $W^s(p)$ and, hence, returns to $p$ in a spiraling fashion. Under suitable genericity conditions [27, 40, 54], this homoclinic bifurcation is of codimension one, meaning that it happens at an isolated value $\eta^*$ when the single parameter $\eta \in \mathbb{R}$ is changed. There are two possible unfoldings of this bifurcation depending on the sign of the saddle quantity

$$\sigma = \lambda^u + Re(\lambda^s_{1,2}). \tag{3}$$

For $\sigma < 0$ a unique and stable periodic orbit bifurcates when $\Gamma_0$ is broken [40, 54]; this is completely analogous to the case of a homoclinic bifurcation of a planar vector field, and one speaks of a simple Shilnikov bifurcation. Panels (a1), (a2) and (a3) of Fig. 1 show the topological changes of the one-dimensional unstable manifold $W^u(p)$ (red curve) during a simple Shilnikov bifurcation at $\omega = \omega_s^*$ (in the example vector field (4) introduced below in Section 2). The situation before the bifurcation in panel (a1), for $\omega > \omega_s^*$, shows how $W^u(p)$ first makes an excursion and subsequently misses the equilibrium as it converges to an attracting equilibrium $q$. At the bifurcation, at $\omega = \omega_s^*$, the global manifold $W^u(p)$ converges to $p$ in both directions of time, forming the homoclinic loop $\Gamma_0$ illustrated in Fig. 1(a2). Finally, in panel (a3) for $\omega < \omega_s^*$, a single stable periodic orbit $\Gamma$ (green curve) bifurcates and becomes the $\alpha$-limit set of the upper branch of $W^u(p)$. Note that, near $p$, the linear stable eigenspace $E^s(p)$ (gray disk) is an approximation of the separatrix $W^s(p)$. In all cases, the other branch of $W^u(p)$ always converges to $q$. The bifurcating periodic orbit $\Gamma$ only exists for $\omega < \omega_s^*$. This is illustrated in the bifurcation diagram in panel (b1), which shows the period $T$ of $\Gamma$ as it grows to infinity when $\omega$ is increased towards $\omega_s^*$. At the limit for $\omega = \omega_s^*$, the periodic orbit becomes the homoclinic orbit $\Gamma_0$ and it no longer exists for $\omega > \omega_s^*$.

The unfolding for $\sigma > 0$ in panels (c1)–(c3) of Fig. 1, on the other hand, is not as straightforward. While the behavior of $W^u(p)$ before and at the Shilnikov bifurcation, as shown in Fig. 1 (c1) and (c2), is similar to that for the simple case, the situation after the bifurcation is not immediately clear. In Fig. 1(c3) the manifold $W^u(p)$ makes two excursions before converging to $q$, but this is just an example of what may happen. More complicated behavior is expected to occur for $\omega$ near the bifurcation value $\omega = \omega_c^*$. Indeed, the Poincaré map constructed near $\Gamma_0$ contains countably many Smale horseshoes in its dynamics, whose suspensions form a compact hyperbolic invariant chaotic set $\mathcal{S}$, which is also referred to as a chaotic saddle [27, 40, 52, 53, 54, 62]. Moreover, the chaotic saddle $\mathcal{S}$ contains countably many periodic orbits $\{\Gamma_k\}_{k\in\mathbb{Z}}$ of saddle type of many possible periods in any sufficiently small neighborhood of $\Gamma_0$ [27, 40, 62]. For system (4), $\mathcal{S}$ is of saddle type and, consequently, in the three-dimensional phase space one expects to see orbits visiting $\mathcal{S}$ in long chaotic transients before they 'settle down' to the attracting equilibrium $q$ or to possible attracting periodic orbits [27]. Furthermore, the existence of a chaotic saddle $\mathcal{S}$ is a robust property, meaning that chaotic dynamics persists on both sides of the bifurcation when the homoclinic orbit is broken [40].

Further global phenomena are expected to happen near the initial Shilnikov homoclinic bifurcation, as $\omega$ is decreased from $\omega_c^*$. Namely, the unstable manifold $W^u(p)$ may form a new connection to the saddle-focus after one or more close encounters with $p$, as is suggested by panel (c3) in Fig. 1. One speaks of subsidiary $n$-homoclinic orbits if the connection back to $p$ occurs only after $n-1$ close passes near it; see [24, 58, 62] for details. Moreover, for each of these subsidiary $n$-homoclinic bifurcations, we have the corresponding scenario with countably many horseshoes as for the primary Shilnikov bifurcation.

Figure 1(b2) shows the (local) bifurcation diagram of the main branch of periodic orbits, bifurcating from the homoclinic orbit at $\omega = \omega_c^*$. In a way, the bifurcation analysis of this 'basic' branch is well known, including how the branch of periodic orbits approaches homoclinicity; see [23, 24, 62] for details. The bifurcation curve in panel (b2) oscillates around $\omega = \omega_c^*$ (compare with the simple case in panel (b1)) with an amplitude that decreases rapidly as the homoclinic limit is approached when $\omega$ tends to $\omega_c^*$. At each of the infinitely many folds of the curve a pair of periodic orbits is created via a saddle-node bifurcation of limit cycles; the periodic orbits $\Gamma_{\mathbf{A}}$ (green dot), $\Gamma_{\mathbf{B}}$ (cyan dot) and $\Gamma_{\mathbf{C}}$ (magenta dot) labeled in Fig. 1(b2) are coexisting examples from this branch for fixed $\omega = -0.83$. Some of the periodic orbits, such as $\Gamma_{\mathbf{B}}$, undergo period-doubling bifurcations (in the case of $\Gamma_{\mathbf{B}}$, this occurs at the points $PD_1$ and $PD_2$) changing their stability along the bifurcation curve. Nevertheless, in a sufficiently small neighborhood of $\omega = \omega_c$ these periodic orbits have two Floquet multipliers of magnitudes less and greater than 1, respectively, and hence, they are all

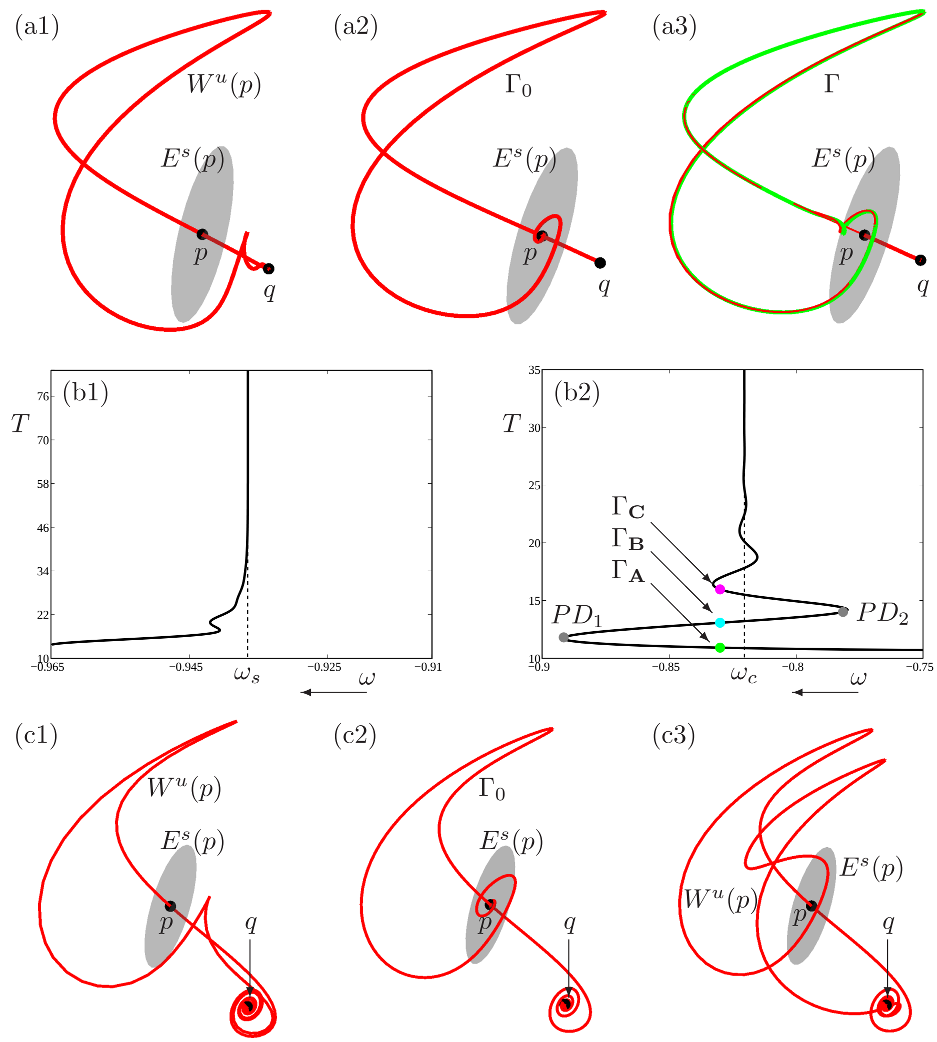


Figure 1: Illustration of the simple and the chaotic Shilnikov bifurcation in system (4). Panels (a1)–(a3) show the one-dimensional unstable manifold $W^u(p)$ (red curve) before, at and after the simple Shilnikov bifurcation for $k = 0.45$ and $\omega = -0.91$, $\omega = \omega_s^* \approx -0.936533$ and $\omega = -0.9419$, respectively; also shown in panel (a3) is the bifurcating periodic orbit $\Gamma$ in green. Panel (b1) shows the associated bifurcation diagram, where the period $T$ of $\Gamma$ is plotted as a function of $\omega$. Panel (b2) shows the corresponding bifurcation diagram for the chaotic Shilnikov bifurcation; three simultaneously existing periodic orbits $\Gamma_{\mathbf{A}}$ (green dot), $\Gamma_{\mathbf{B}}$ (cyan dot) and $\Gamma_{\mathbf{C}}$ (magenta dot) are highlighted. Panels (c1)–(c3) show $W^u(p)$ before, at and after the chaotic Shilnikov bifurcation for $k = 0.7$ and $\omega = -0.81$, $\omega = \omega_c^* \approx -0.820455$ and $\omega = -0.83$, respectively.

hyperbolic periodic orbits of saddle type. The Floquet mulipliers may either be both positive or both negative, and then the associated periodic orbit has either orientable or non-orientable two-dimensional stable and unstable manifolds. The sign of the Floquet mulipliers, and hence the orientability of the associated manifolds, actually alternates between consecutive periodic orbits if $\omega$ is close enough to the value $\omega_c$ where the homoclinic bifurcation takes place. For instance, near $\omega = \omega_c$, $\Gamma_{\mathbf{A}}$ and $\Gamma_{\mathbf{C}}$ have positive Floquet multipliers and $\Gamma_{\mathbf{B}}$ has negative Floquet multipliers; see [47] for details. Notice further that, as $\omega$ is varied from $\omega_c$, the manifold $W^u(p)$ may intersect the stable manifold $W^s(\Gamma_k)$ of any periodic orbit $\Gamma_k$ to form codimension-one heteroclinic connections (also known as EtoP connections [38]).

### 1.3 The role of two-dimensional invariant manifolds

Figure 1 shows the Shilnikov bifurcations on the level of the reorganization of the one-dimensional manifolds involved; this is what one can typically find in literature [23, 24, 52, 53, 54, 62]. The presence of Shilnikov chaos has been determined by means of defining a Poincaré map on suitable cross-sections near the homoclinic orbit $\Gamma_0$, which is then further reduced to a one-dimensional map [52, 53, 62]. This approach is perfect for proving statements about the dynamics near the Shilnikov bifurcation. On the other hand, it is less clear how the dynamics that is found in this way manifest itself throughout phase space.

In this paper we focus on the role of the two-dimensional manifolds as organizers of the overall dynamics. Historically, the two-dimensional invariant manifolds associated with homoclinic phenomena have been considered locally near the equilibrium or in a tubular neighborhood of the connecting orbit $\Gamma_0$, mainly via intersections with a local section or in the form of topological sketches [40, 54, 62]. We know, for instance, that the closure of the stable manifold of the saddle-focus is locally disconnected at the Shilnikov bifurcation [48]. However, the question that remains open for both cases of Shilnikov bifurcation is how the associated stable manifolds rearrange themselves during the homoclinic bifurcation. More specifically, our aim is to answer the following questions:

- How does the topological change due to the Shilnikov bifurcation manifest itself in terms of the global geometry of $W^s(p)$?
- How do the basins of the attracting objects change in the simple Shilnikov case?
- What are the roles of $W^s(p)$ and $W^s(\Gamma_k)$ in the organization of phase space in the presence of the chaotic saddle $\mathcal{S}$?

These questions are of special interest, because Shilnikov bifurcations have been found as important ingredients of the dynamics in many concrete applications; examples include laser models [39, 59, 58]; nerve impulse propagation in neurons and axons [31]; travelling waves in the FitzHugh-Nagumo model with slow-fast dynamics [28]; models for chaos-based communication systems [57]; electrochemical reactions [4] and oxidation processes [44]; electrodynamic convection in liquid crystals [49]; food chain models in predator-prey systems [56]; nonlinear convection in magnetic fields [50]; and the Rössler equations [3]. In these applications, knowing the stable manifold of the saddle-focus is especially relevant, because it acts as a threshold for excitability: a small perturbation above $W^s(p)$ leads to an excursion following the unstable manifold $W^u(p)$ before converging to a nearby attractor ($q$ in Fig. 1, which is for the laser model (4) that we shall introduce in Section 2). The effect is a pulse-like response in relevant state variables. Multipulse behavior is also possible, meaning that several pulses or responses may be generated from a single perturbation above the threshold [39, 60, 58, 62].

Although there is no normal form for homoclinic bifurcations (or any other global bifurcations for that matter), the applications mentioned above (and many others) provide a rich set of model vector fields from which one can select a concrete example showing both the simple and the chaotic Shilnikov cases. We consider here the model for a laser with optical injection from [59] as a convenient system in which to analyze the roles of the two-dimensional stable manifolds involved in the organization of its three-dimensional phase space. This study is possible thanks to the emergence of advanced numerical methods for the accurate computation of two-dimensional global invariant manifolds. We follow the approach from [36] and obtain the respective two-dimensional manifolds by continuing a one-parameter family of orbit segments, which can be found as solutions of a suitable two-point boundary value problem, for example, with the package AUTO [18]. A brief discussion of these numerical methods is presented in the Appendix of this paper, and we refer to [36, 37] for further details. We take advantage of the flexibility of this computational technique to calculate also the intersection curves of the manifolds with a suitable two-dimensional surface [1, 16]. More specifically, we initially consider the classical approach of taking a plane $\Sigma$ through the equilibrium $p$; in this way, for the simple Shilnikov bifurcation we discover that $W^s(p)$ is a bounded surface that accumulates on a repelling strange set. However, we mainly study the intersections of the respective two-dimensional global manifolds with a sphere $S_R$ of radius $R$ centered at $p$.

The advantage of the sphere $S_R$ is that it is compact, which allows us to study in a convenient way how the basins of attraction of $q$ and $\Gamma$ change as their boundaries, formed by different portions of $W^s(p)$, rearrange themselves at the simple Shilnikov bifurcation. Provided $R$ is chosen small enough, we find that there are only two intersection curves of $W^s(p)$ with $S_R$ (provided $R$ is small enough); one accumulates on the other at the homoclinic bifurcation, and this changes the topology of the regions they bound on the sphere. For the chaotic Shilnikov bifurcation, on the other hand, there are infinitely many intersection curves between $W^s(p)$ and $S_R$; they are nested before the bifurcation, and this nesting property is progressively lost after the bifurcation in a sequence of transitions that all involve the analogous rearrangement of closed curves that we found for the simple Shilnikov bifurcation. Moreover, we find that the stable manifolds $W^s(\Gamma_k)$ of the saddle periodic orbits $\Gamma_k$ (which are part of the chaotic saddle $\mathcal{S}$) accumulate on $W^s(p)$ and, hence, are organised and bifurcate in the same way; in particular, we identify $W^s(p)$ as the accessible boundary of the basin of attraction of the equilibrium $q$.

This paper is structured as follows. In Section 2 we present the laser model that is used throughout for the analysis of the Shilnikov bifurcation. The study of the simple Shilnikov bifurcation is presented in Section 3, where we also introduce our approach of computing and visualizing suitable intersection curves of $W^s(p)$. The chaotic Shilnikov bifurcation is studied in Section 4, where we show in turn how the stable manifolds $W^s(p)$ of the saddle-focus $p$ and $W^s(\Gamma_k)$ of the saddle periodic orbits $\Gamma_k$ organize the phase space in the presence of a chaotic saddle. In Section 5 we briefly summarize the main results, discuss their consequences and outline some challenges for future work. The Appendix presents an overview of the boundary-value-problem implementation that we used to compute two-dimensional invariant manifolds of saddle equilibria and periodic orbits.

## 2 The laser model

We consider here the laser model with optical injection derived in [59]. We write the system of equations as

$$\left\{ \begin{array}{rcl} \dot{x} &=& \omega y + \frac{1}{2}\, x\, z - \frac{a}{2} y\, z + k, \\ \dot{y} &=& -\omega x + \frac{1}{2}\, y\, z + \frac{a}{2}\, x\, z, \\ \dot{z} &=& -2\, G\, z - (1 + 2\, B\, z)(x^2 + y^2 - 1), \end{array} \right. \tag{4}$$

where $(x, y, z) \in \mathbb{R}^3$. Here, $x$ and $y$ denote the real and imaginary parts of the complex electric field, respectively, and $z$ the population inversion, i.e., the number of electron-hole pairs in the case of a semiconductor laser. This model describes a single-mode laser that receives optical injection at amplitude $k$ and detuning $\omega$; furthermore, $a$, $B$ and $G$ describe material properties of the laser; for our purposes, they are fixed throughout at the realistic values $a = 2$, $B = 0.015$ and $G = 0.035$.

An extensive bifurcation analysis of the laser model (4) can be found in [58] where, among several kinds of global bifurcations, many curves of Shilnikov homoclinic bifurcations to a saddle-focus $p$ were found in the $(k, \omega)$-plane for different values of the parameter $a$. The study in [58] focused mainly on the complicated structure of curves of $n$-homoclinic bifurcations as the parameter $a$ is varied, and their physical relevance as a means for understanding multipulse excitability of the laser. Figure 2 shows one such curve, obtained by continuation of the homoclinic orbit $\Gamma_0$ using the HomCont [9] part of the continuation package Auto [18]. The tooth-like curve $h$ of (primary) 1-homoclinic orbits connects the points $A_1$ and $A_2$ in Fig. 2, where it becomes tangent to a saddle-node bifurcation curve $SN$. The saddle quantity $\sigma$, defined in (3), of the equilibrium $p$ changes sign across the dashed neutral-saddle curve labeled $ns$. Along $h$, the Shilnikov homoclinic bifurcation is simple to the left of $ns$ and chaotic to the right of $ns$. The transition between simple and complicated dynamics occurs at so-called Belyakov points, labeled $B_1$ and $B_2$ in Fig. 2, which are precisely the points where $h$ intersects $ns$, so that $\sigma = 0$; see also [6, 58]. At all other points of the curve $h$ the Shilnikov homoclinic bifurcation is of codimension one; this means that (except at the fold of $h$ with respect to $\omega$) it happens at an isolated value $\omega = \omega^*$ when the single parameter $\omega \in \mathbb{R}$ is changed. This allows us to unfold the bifurcation by keeping a fixed value of $k$ and just changing $\omega$ through $\omega^*$.

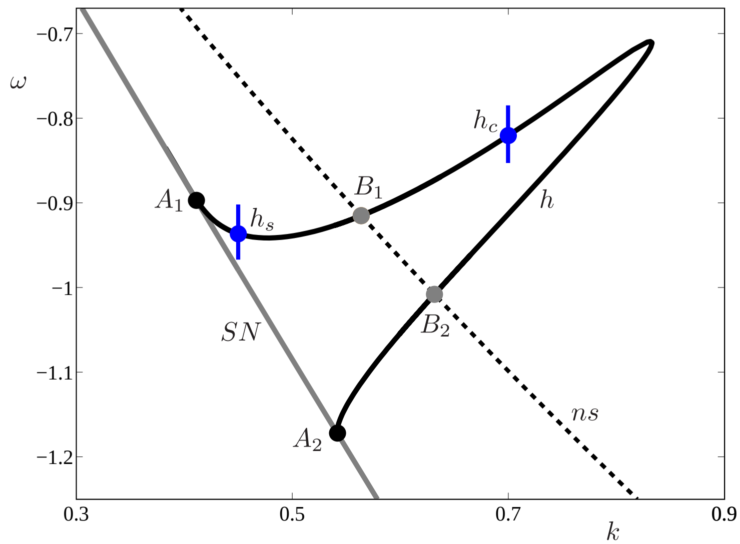


Figure 2: The laser system (4) has a tooth-shaped curve $h$ of primary Shilnikov homoclinic bifurcations in the $(k, \omega)$-plane; the curve $h$ starts and ends at the points $A_1$ and $A_2$ on a saddle-node bifurcation curve $SN$. At the selected points $h_s$ and $h_c$ one finds a simple and a chaotic Shilnikov bifurcation, respectively, which can be unfolded by changing only the parameter $\omega$. The transition between the two cases occurs at the Belyakov points $B_1$ and $B_2$, where the curve $h$ intersects the neutral saddle curve $ns$.

To the right of the curve $SN$ there is a saddle equilibrium $p$ and a stable equilibrium point, denoted $q$, which has a large basin of attraction $\mathcal{B}(q)$ that is bounded by the two-dimensional manifold $W^s(p)$. The existence of an attractor $q$ is not part of the classical theory of Shilnikov bifurcation, which only considers the saddle $p$ and a tubular neighborhood of the homoclinic orbit $\Gamma_0$. In system (4) the attractor $q$ absorbs orbits that leave a neighborhood of the Shilnikov homoclinic orbit. This allows us to gain insight into the bifurction by studying the properties of the basin $\mathcal{B}(q)$. Specifically, we study how the interaction of $\mathcal{B}(q)$ and $W^s(p)$ gives rise to the basin $\mathcal{B}(\Gamma)$ of the bifurcating saddle periodic orbit $\Gamma$ in the simple Shilnikov bifurcation; and how, near a chaotic Shilnikov bifurcation, the boundary of $\mathcal{B}(q)$ is formed in a complicated way by $W^s(p)$ and by the stable manifolds of the periodic orbits of saddle type.

In the following sections, we consider two specific points on the curve $h$ in Fig. 2 where we find the simple and chaotic cases of Shilnikov homoclinic bifurcations:

- At $h_c = (k_s^*, \omega_s^*) \approx (0.45, -0.936533)$ the saddle-focus $p \approx (0.728926, 0.716564, -0.716563)$ has associated eigenvalues $\lambda_{1,2}^s = -0.452133 \pm 1.11566\, i$ and $\lambda^u = 0.205017$. Hence, the saddle quantity $\sigma$ is negative and one is dealing with a

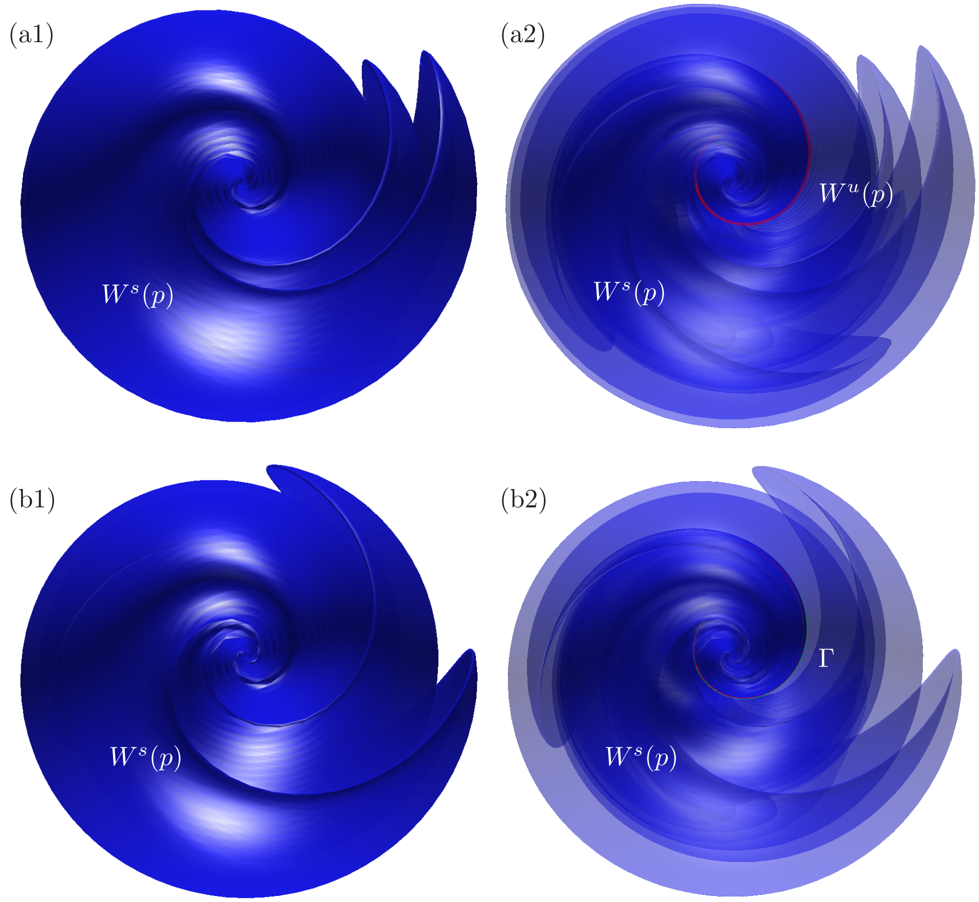


Figure 3: The two-dimensional stable manifold $W^s(p)$ before (row (a) for $\omega = -0.93$) and after (row (b) for $\omega = -0.94$) the simple Shilnikov homoclinic bifurcation in (4) for $k = 0.45$. The manifold is represented by orbit segments of fixed integration time $T_0 = 40$, and the viewpoint lies on the $z$-axis above the $(x, y)$-plane; in the right panels $W^s(p)$ is rendered as a transparent surface.

simple Shilnikov bifurcation; see Fig. 1(a1)–(a3).

- At $h_c = (k_c^*, \omega_c^*) \approx (0.7, -0.820455)$ the eigenvalues of $p \approx (0.0910993, 1.00029, -0.126416)$ are $\lambda_{1,2}^s = -0.417498 \pm 1.3632\,i$ and $\lambda^u = 0.638313$. Hence, $\sigma > 0$ and one is dealing with a chaotic Shilnikov bifurcation; see Fig. 1(c1)–(c3).

## 3 The simple Shilnikov bifurcation

We first study the role of the stable manifold $W^s(p)$ of the saddle-focus $p$ in the laser model (4) near the simple Shilnikov homoclinic bifurcation for $k = 0.45$. Figure 3 shows $W^s(p)$ computed as a one-parameter family of orbit segments of fixed integra-

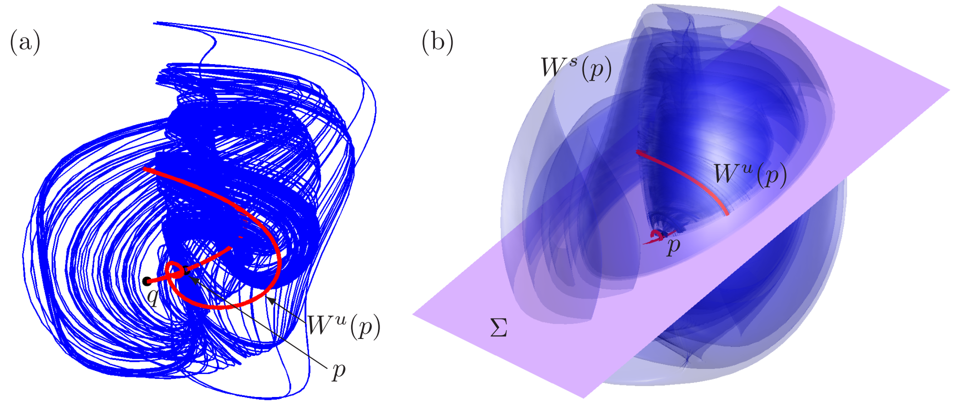


Figure 4: Illustration of $W^s(p)$ for $\omega = -0.93$ and $k = 0.45$. Panel (a) shows a single computed orbit segment in $W^s(p)$. Panel (b) shows $W^s(p)$ as a transparent surface from a different viewpoint that highlights the structure of its layers; also shown is a global planar section $\Sigma$ through $p$.

tion time $T_0 = 40$, one end point of which lies in $E^s(p)$ at a distance of the order of $10^{-5}$ from $p$; see the Appendix for details. Panels (a1) and (a2) of Fig. 3 show $W^s(p)$ before the Shilnikov bifurcation for $\omega = -0.93$, and panels (b1) and (b2) show it after the Shilnikov bifurcation for $\omega = -0.94$; in each case, the blue surface $W^s(p)$ is shown in both solid (left) and transparent (right) rendering from a viewpoint on the $z$-axis above the $(x, y)$-plane.

Figure 3 illustrates that the computed piece of $W^s(p)$, which is a topological disk, has a quite complicated, shell-like geometry. The rotational component of the vector field near the saddle-focus $p$ induces a swirling behavior of $W^s(p)$. Moreover, the surface has several layers, which may be very close to each other and separate the phase space locally into different regions. Figure 3 gives an idea that the global geometry of $W^s(p)$ is quite intriguing, but it does not illustrate very well where $W^s(p)$ lies in relation to the unstable manifold $W^u(p)$ and the saddle-focus $p$, and what topological change this manifold undergoes at the homoclinic bifurcation.

Figure 4 further illustrates the properties of $W^s(p)$ for $\omega = -0.93$ before the bifurcation; recall that the equilibrium $q$ is the only attractor, so that all points not on $W^s(p)$ end up at $q$ under the flow of (4). Figure 4(a) shows how a single orbit in $W^s(p)$ spends a long time in a transient motion before finally reaching $p$. This gives a hint of the influence of the different layers of $W^s(p)$, which induce a similarly complicated transient behavior of nearby orbits in the basin of the attractor $q$. Figure 4(b) shows $W^s(p)$ as a transparent surface, from the same viewpoint as panel (a), which clearly shows the different layers.

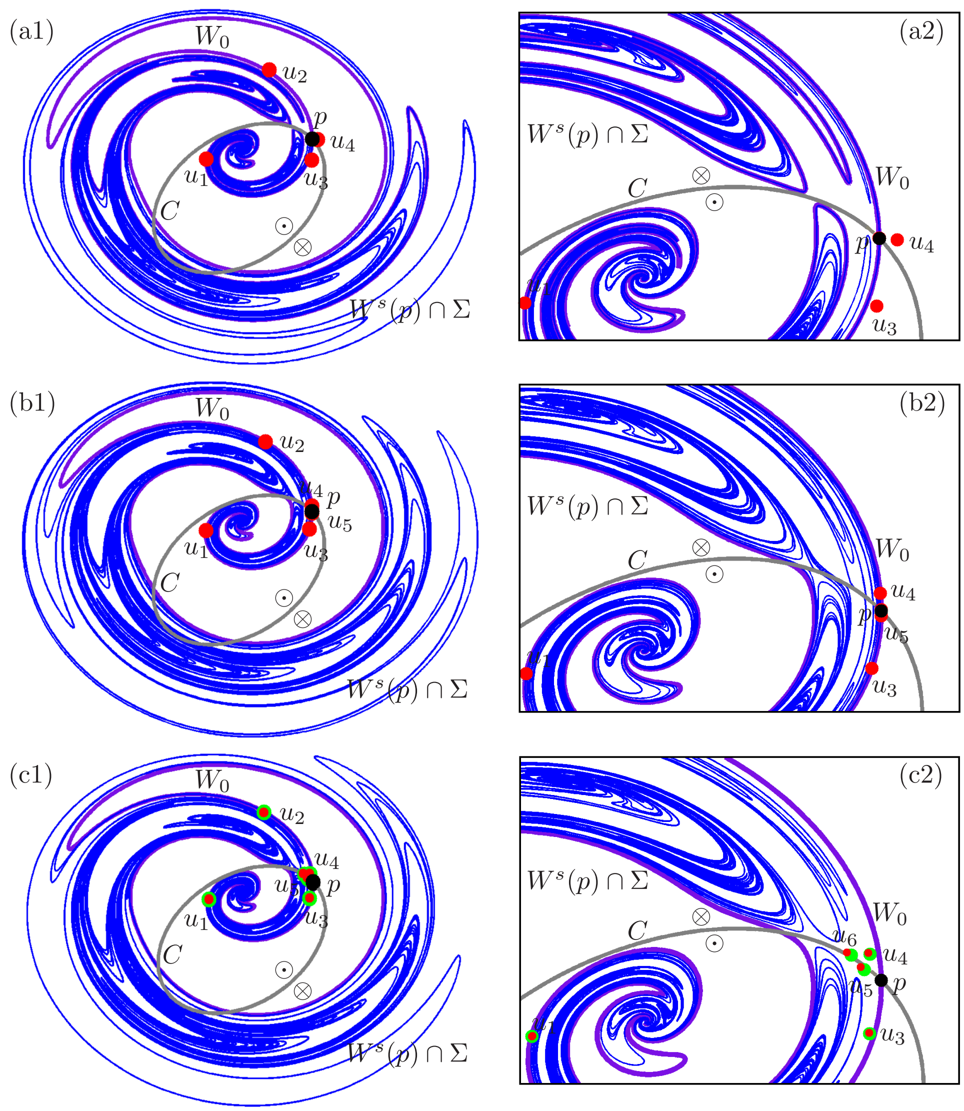


Figure 5: Organization of stable (blue curves) and unstable manifolds (red dots) in the planar section $\Sigma$ through the equilibrium $p$ before (row (a) for $\omega = -0.93$), approximately at (row (b) for $\omega = \omega_s^* \approx -0.936533$), and after (row (c) for $\omega = -0.94$) the simple Shilnikov bifurcation for $k = 0.45$ in the laser model (4); the right panels are enlargements near $p$. The darker blue curve $W_0 \subset W^s(p) \cap \Sigma$ is the unique intersection curve that contains $p$. Along the tangency locus $C$ the vector field changes direction (w.r.t. the normal to $\Sigma$) between pointing up ($\odot$) and down ($\otimes$).

### 3.1 Intersection of $W^s(p)$ with a planar section

In order to get an impression of the complicated arrangement of layers of $W^s(p)$ near the simple Shilnikov bifurcation at $\omega_s^*$, we first follow the classical approach and consider its intersection with a planar section through the equilibrium $p$. Figure 4(b) shows such a section $\Sigma$, namely, the plane through $p$ spanned by the unstable eigenvector $\mathbf{v}^u$ and a vector $\mathbf{v}^s$ in $E^s(p)$. Figure 5 shows the corresponding intersection sets of invariant manifolds with $\Sigma$ before, at and after the bifurcation in rows (a)–(c), respectively. More specifically, shown are the set $W^s(p) \cap \Sigma$ (blue curves), the set $\{u_i\}_i := W^u(p) \cap \Sigma$ (red dots) and, in row (c) after the bifurcation, the intersection points $\Gamma \cap \Sigma$ (green dots). The curves in $W^s(p) \cap \Sigma$ have been computed by continuing orbit segments whose begin points lie in $\Sigma$ and whose end points lie near $p$ in $E^s(p)$; see the Appendix for details. Also shown in Fig. 5 is the tangency locus $C \subset \Sigma$ where the vector field (4) is tangent to $\Sigma$; it is given by

$$C := \{\mathbf{x} \in \Sigma \,|\, f(\mathbf{x}) \cdot \vec{n}_\Sigma = 0\}, \tag{5}$$

where $\vec{n}_\Sigma$ is the unit normal vector to $\Sigma$. The relevance of $C$ is that it divides $\Sigma$ into two regions where the flow points upwards (in the direction of positive $z$) or downwards (in the direction of negative $z$); this is indicated with the symbols $\odot$ and $\otimes$, respectively. The first-return map to the global section $\Sigma$ is not a diffeomorphism [41], and this has some interesting consequences. In particular, $W^s(p) \cap \Sigma$ is not a single curve, but consist of infinitely many curves. Note that many of these curves in $W^s(0) \cap \Sigma$ cross the tangency locus $C$; nevertheless, they can be computed reliably [19]. The special curve containing the equilibrium $p$ is labeled $W_0$ and colored a darker blue; note that $p \in \Sigma$ implies that $p \in C$. The intriguing geometry of the many layers of $W^s(p)$ is a feature both before and after the Shilnikov bifurcation. The fact that we find infinitely many bounded curves in $W^s(p) \cap \Sigma$ implies that $W^s(p)$ is a bounded surface that converges (in backward time) to a chaotic repellor. In other words, the orbit through a generic point in $\Sigma$ returns many times to $\Sigma$, while visiting different regions bounded by curves in $W^s(p) \cap \Sigma$, until it eventually converges to either $q$ or to $\Gamma$.

Figure 5 illustrates the interaction between the manifolds $W^s(p)$ and $W^u(p)$ on the level of their intersection sets with the plane $\Sigma$. Before the simple Shilnikov bifurcation, the set $W^u(p) \cup \Sigma$ consists of only finitely many points, namely the four points $u_1, \ldots u_4$ in panel (a1). These points lie in the intersection with $\Sigma$ of the basin $\mathcal{B}(q)$ of the attracting equilibrium $q$, which consists of $\Sigma \setminus W^s(p)$. At the bifurcation, in row (b), there are infinitely many points $u_i \in W^u(p) \cup \Sigma$, which lie on the curve $W_0 \subset W^s(p) \cap \Sigma$ and converge to $p$. After the bifurcation, in row (c) of Fig. 5, there are still infinitely many points $u_i \in W^u(p) \cup \Sigma$, but they now lie on the other side of $W_0$ and accumulate on the intersection points $\Gamma \cap \Sigma$ of the bifurcating periodic orbit $\Gamma$ with $\Sigma$. In particular, this implies that the plane $\Sigma$ must be divided by $W^s(p) \cap \Sigma$ into its intersection with the basin of $q$ and its intersection with the basin of $\Gamma$, respectively. Note, however, that it is not at all clear which of the two basins is where, and one cannot decide from Fig. 5 how $W^s(p)$ changes topologically at the simple Shilnikov bifurcation. The enlargement panels (right column) of Fig. 5

show that there are some rearrangements of $W^s(p) \cap \Sigma$, but it is not clear which of these rearrangements happen directly at the Shilnikov bifurcation. The problem is that, as the parameter is changed, curves in $W^s(p) \cap \Sigma$ may reconnect differently in tangency bifurcations that take place at isolated points on $C$ (away from $p$). This type of bifurcation in the section $\Sigma$ is a consequence of the presence of the tangency locus $C$, and such a tangency bifurcation of $W^s(p) \cap \Sigma$ is generally not a bifurcation of the two-dimensional invariant manifold $W^s(p)$ itself; see [41] for more details.

The issues outlined above highlight the need for a better representation and visualization of the global manifolds involved.

### 3.2 Intersection of $W^s(p)$ with a sphere

The topological change of $W^s(p)$ during the simple Shilnikov bifurcation becomes much easier to understand when one considers its intersection with a suitable sphere around the saddle-focus $p$. We consider the sphere

$$S_R = \{(x, y, z) \in \mathbb{R}^3 \,|\, (x - p_x)^2 + (y - p_y)^2 + (z - p_z)^2 = R^2\}$$

centered at the equilibrium point $p = (p_x, p_y, p_z)$, where we choose $R = 0.5$ as a suitable radius. Figure 6 shows how a strip of $W^s(p)$ (blue surface) returns (in backward time) to the sphere $S_R$, while following the upper branch of $W^u(p)$ (red curve). Here rows (a) and (b) show the situations before and after the simple Shilnikov bifurcation, respectively; also shown in green in row (b) is the periodic orbit $\Gamma$. Panels (a1) and (b1) show only the strip that returns to $S_R$, while panels (a2) and (b2) show how it is situated within the entire (transparent) stable manifold $W^s(p)$. Note, in particular, that $W^u(p)$ moves from one side of the strip of $W^s(p)$ to the other at the bifurcation.

The idea is now to consider only the intersection sets of the relevant manifolds with the sphere $S_R$, which can be computed readily by restricting the continuation to orbit segments whose end points (in backward time) lie on $S_R$; see the Appendix for details. It turns out that the set $\widehat{W}^s(p) := W^s(p) \cap S_R$ consists of only two curves $W_0$ and $W_1$ before, at and after the bifurcation (provided $R$ is sufficiently small). More specifically, $W_0 := W^s_{\mathrm{loc}}(p) \cap S_R$ is the first intersection of $W^s(p)$ with $S_R$. It is a simple closed curve that bounds a disk formed by the part of $W^s_{\mathrm{loc}}(p)$ inside $S_R$. All points on $W_0$ flow directly to $p$, that is, the vector field along $W_0$ points into the sphere $S_R$. The second intersection curve $W_1$ is formed by a portion of $W^s(p)$ that re-enters $S_R$ (in backward time) and leaves again, containing points where the flow is tangent to $S_R$; the blue strip in Fig. 6 is a portion of $W^s(p)$ that gives rise to $W_1$. Figure 7 shows the situation on $S_R$ approximately at the Shilnikov bifurcation for $\omega = \omega_s^*$; panel (a) shows the intersection curves on the sphere, with parts of the region of interest obscured due to the choice of viewpoint. Figure 7(b) shows a stereographic projection of the sphere onto the $(u, v)$-plane tangent to $S_R$ at the north pole $N = (p_x, p_y, p_z + R)$, which is given by the transformation

$$(u, v) := \left( -\frac{R\,(y - p_y)}{R + z - p_z}, \frac{R\,(x - p_x)}{R + z - p_z} \right), \tag{6}$$

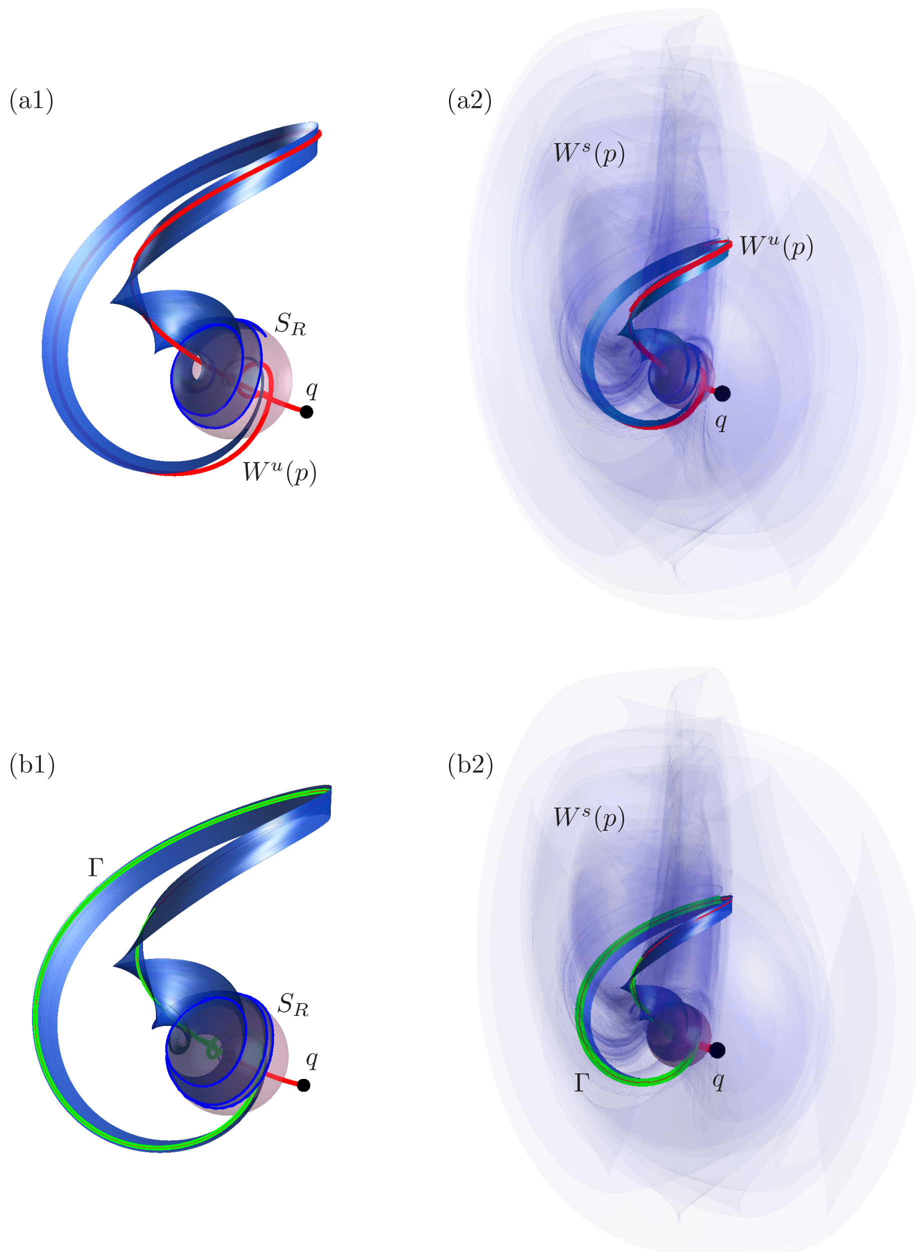


Figure 6: A (blue) strip of orbit segments on $W^s(p)$ (blue transparent surface) returning (in backward time) to the sphere $S_R$ with radius $R = 0.5$, shown before (row (a) for $\omega = -0.93$) and after (row (b) for $\omega = -0.94$ ) the simple Shilnikov bifurcation in (4) for $k = 0.45$; also shown are $W^u(p)$ (red curve) and $\Gamma$ (green curve).

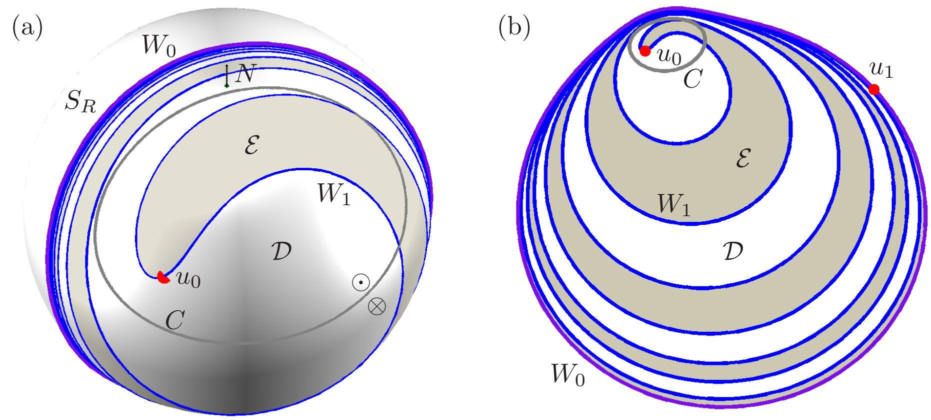


Figure 7: The intersection curves $W_0$ (dark blue) and $W_1$ (blue) of $W^s(p) \cap S_R$ for $k = 0.45$ and $\omega = \omega_s^* \approx -0.936533$, shown on the sphere $S_R$ (a) and in stereographic projection (b); also shown is the tangency locus $C$, where the direction of the vector field changes between pointing out of $S_R$ ($\odot$) and into $S_R$ ($\otimes$).

where $(x, y, z) \in S_R$. The closed curve $W_0$ (shown in a darker blue) divides $S_R$ into two regions, one of which contains $W_1$. Note that the two points $\{u_0, u_1\} = \widehat{\Gamma}_0 := W^u(p) \cap S_R$ lie on $W_1$ and $W_0$, respectively. The stereographic projection clearly shows how $W_1$ accumulates on $W_0$, which forms the boundary of the region of interest on $S_R$. The orbit of a point on the outside of $W_0$ in Fig. 7(b) converges directly to the attractor $q$ without intersecting $S_R$ again. Points inside $W_0$, on the other hand, have orbits that move 'in between' the layers of $W^s(p)$ before converging to $q$.

Also shown in Fig. 7 is the tangency locus $C \subset S_R$, now given by

$$C := \{\mathbf{x} \in S_R \,|\, f(\mathbf{x}) \cdot \vec{n}_{S_R}(\mathbf{x}) = 0\}, \tag{7}$$

where $\vec{n}_{S_R}(\mathbf{x})$ is the unit normal vector to $S_R$ at $\mathbf{x}$. Notice that $C$ is quite far from the accumulation of $W_1$ on $W_0$. Hence, in contrast to the planar section $\Sigma$, there is no evidence of tangency bifurcations on the sphere $S_R$ near the simple Shilnikov bifurcation.

We now turn to the question of how $W_0$ and $W_1$ change topologically at the simple Shilnikov bifurcation. The region inside $W_0$ in Fig. 7 is subdivided by $W_1$ into two regions labelled $\mathcal{D}$ and $\mathcal{E}$. Their roles become clear in Fig. 8, where we show how $W_1$ changes topologically through the Shilnikov bifurcation. The situation before the bifurcation is illustrated in panels (a)–(c) for three values of $\omega$ approaching $\omega_s^*$, while panels (d)–(f) show the situation after the bifurcation for three values of $\omega$ decreasing from $\omega_s^*$. Panels (a1)–(f1) of Fig. 8 show the stereographic projection of the relevant sets on the sphere $S_R$. In each panel, $W_0$ is the darker blue curve that bounds the region of interest in which one finds $W_1$.

Before the simple Shilnikov bifurcation, the upper branch of $W^u(p)$ leaves the

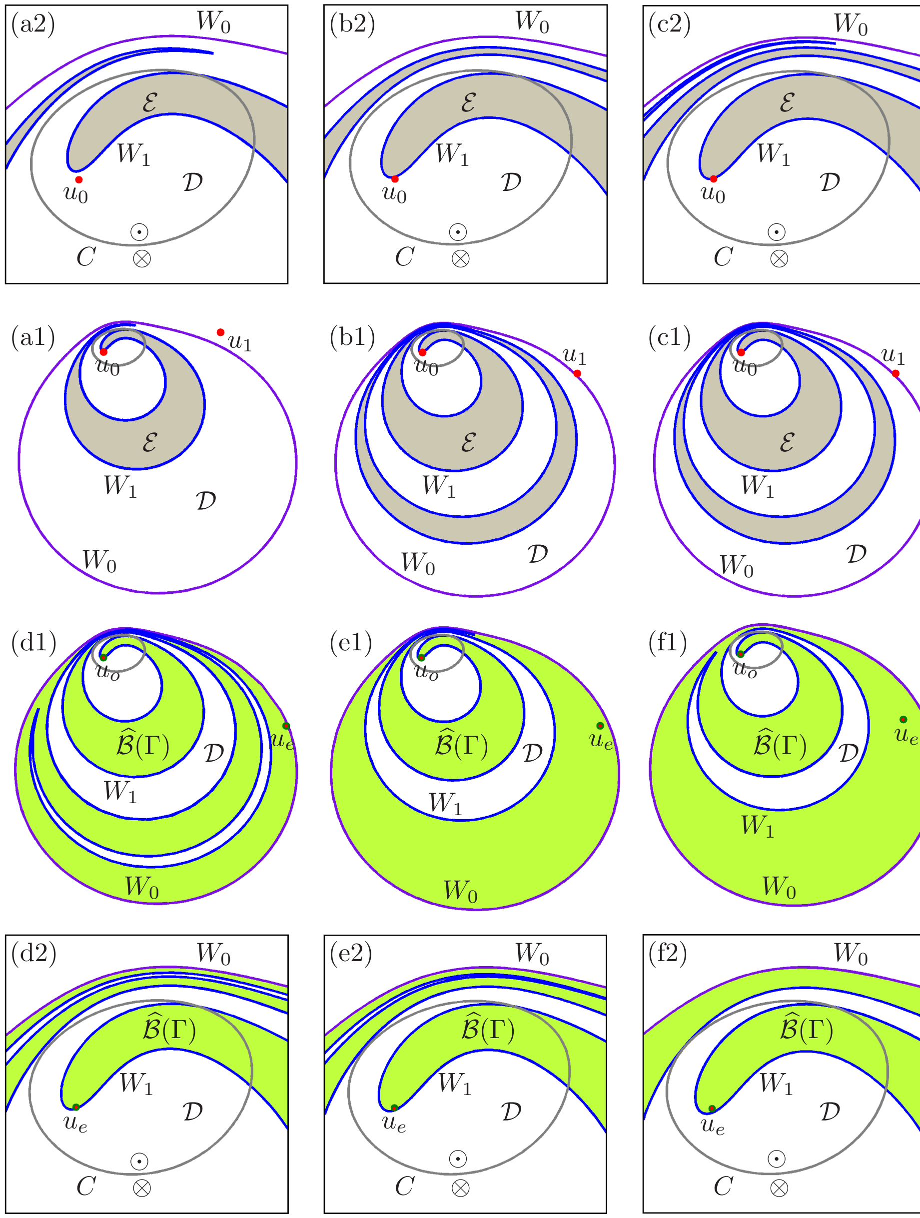


Figure 8: Stereographic projection of $\widehat{W}^s(p) = \{W_0, W_1\}$ near a simple Shilnikov bifurcation (a1)–(f1); panels (a2)–(f2) are enlargements near $u_0 \in \widehat{W}^u(p)$. Panels (a)–(c) for $\omega \in \{-0.93, -0.935, -0.936\}$ are before, and panels (d)–(e) for $\omega \in \{-0.937, -0.938, -0.94\}$ are after the bifurcation for $k = 0.45$. The inside of $W_0$ is divided into the regions $\mathcal{D}$ and $\mathcal{E}$; after the bifurcation $\mathcal{E}$ becomes the basin $\widehat{\mathcal{B}}(\Gamma)$.

sphere $S_R$ at the (red) point $u_0$ inside the closed tangency curve $C$, and it re-enters

$S_R$ at the (red) point $u_1$. The manifold then leaves $S_R$ again to converge to $q$; this final intersection point $u_2$ is far away from the shown region of interest and is not depicted in Fig. 8(a1)–(c1). The basin $\widehat{B}(q) := \mathcal{B}(q) \cap S_R$ of the only attractor $q$ is the complement of $\widehat{W}^s(p) = \{W_0, W_1\}$. Notice that, before the bifurcation, $W_1$ is a closed curve that divides the region of interest inside $W_0$ into two simply connected regions: the region $\mathcal{D} \subset \widehat{B}(q)$ that is bounded by both $W_0$ and $W_1$, and the (shaded) region $\mathcal{E} \subset \widehat{B}(q)$ that is bounded only by $W_1$. Orbits of points in $\mathcal{D}$ converge directly to $q$, while orbits of points in $\mathcal{E}$ make an excursion before reaching $q$. As the Shilnikov bifurcation at $\omega_s^*$ is approached, the (red) points $u_0$ and $u_1$ approach $W_1$ and $W_0$, respectively. At the same time, the region $\mathcal{E}$ develops a 'tail' that grows clockwise toward $W_0$; see Fig. 8(a)–(c). At the Shilnikov bifurcation for $\omega = \omega_s^*$ the set $W_1$ is no longer a Jordan curve. Rather $W_1$ is an arc of infinite arclength, both ends of which accumulate on the closed curve $W_0$; this is the situation depicted in Fig. 7(b).

The situation after the simple Shilinikov bifurcation is shown in panels (d)–(f) of Fig. 8. The set $\widehat{W}^u(p) = W^u(p) \cap S_R$ now consists of infinitely many points $\{u_0, u_1, \cdots\}$ that converge very rapidly to the (green) intersection points $\widehat{\Gamma} := \Gamma \cap S_R$ of the bifurcating attracting periodic orbit $\Gamma$; the (indistinguishable) odd-numbered intersection points are indicated by the symbol $u_o$ and the (equally indistinguishable) even-numbered ones by $u_e$. Notice that $W_1$ is again a closed curve that separates the interior of $W_0$ into two simply connected regions, but it has effectively 'turned inside out' at the bifurcation. The (shaded) region bounded by both $W_1$ and $W_0$ is the basin of attraction $\widehat{\mathcal{B}}(\Gamma) := \mathcal{B}(\Gamma) \cap S_R$ of $\Gamma$; hence, this basin emerges as the continuation of the $\mathcal{E} \subset \widehat{B}(q)$ that exists before and at the bifurcation. The region bounded by only $W_1$, on the other hand, is now (the continuation of) region $\mathcal{D} \subset \widehat{B}(q)$. As $\omega$ is increased towards $\omega_s$ and the bifurcation is approached, $\mathcal{D}$ forms a 'tail'. This means, that a small narrow and growing 'inlet' is taken out of $\widehat{\mathcal{B}}(\Gamma)$; see the sequence of panels (f)–(d) of Fig. 8. The result of this convergence process is again the situation at the bifurcation itself that is depicted in Fig. 7(b).

It is an important realization that the topological change we observe at the simple Shilnikov bifurcation does not depend on the choice of the radius $R$ of $S_R$, provided it is small enough. More specifically, for any sufficiently small $R > 0$ there exist a neighborhood $U_R^*$ of $\omega_s^*$ such that $W_0$ and $W_1$ are the only intersection curves in $\widehat{W}^s(p)$ for $\omega \in U_R^*$, and they have the properties we discussed and illustrated in Figs. 8 and Fig. 7(b). Hence, the representation of the invariant global manifolds on the sphere $S_R$ indeed provides the desired insight into the exact topological nature of the simple Shilniov bifurcation. In particular, it explains how the basin of attraction $\widehat{\mathcal{B}}(\Gamma)$ (dis)appears as a big set at the moment of bifurcation.

While these results were obtained for the specific laser model (4), they appear to be an entirely general description of the topological change observed near any simple Shilnikov bifurcation. We formalize this observation as follows.

**Result 1** *(Simple Shilnikov bifurcation) Suppose that the parameter $\eta$ unfolds a simple Shilnikov bifurcation at $\eta = \eta_s^*$ of a saddle-focus $p$ of vector field* (1)*. Then, on any sufficiently small sphere $S_R$ centered at $p$, the set $\widehat{W}^s(p) := W^s(p) \cap S_R$ consists of only two curves, $W_0$ and $W_1$. Furthemore, $W_0 := W^s_{\text{loc}}(p) \cap S_R$ is always* *a closed curve and the following holds:*

*(S.1) For $\eta < \eta_s^*$ (before the bifurcation) $W_1$ is a closed curve that bounds a simply connected region $\mathcal{E}$. As $\eta$ approaches $\eta_s^*$, the arclength of $W_1$ diverges.*

*(S.2) For $\eta = \eta_s^*$ (at the bifurcation) the curve $W_1$ is an arc with infinite arclength, the two ends of which converge to the closed curve $W_0$.*

*(S.3) For $\eta > \eta_s^*$ (after the bifurcation) $W_1$ is again a closed curve with finite arclength. The basin $\widehat{\mathcal{B}}(\Gamma) \subset S_R$ of the bifurcating stable periodic orbit $\Gamma$ is bounded by both $W_0$ and $W_1$. Furthermore, $\widehat{\mathcal{B}}(\Gamma)$ is the continuation (in the Hausdorff metric) of the region $\mathcal{E}$ for $\eta < \eta_s^*$, that is,*

$$\lim_{\eta \nearrow \eta_s^*} \mathcal{E} = \lim_{\eta \searrow \eta_s^*} \widehat{\mathcal{B}}(\Gamma).$$

## 4 The chaotic Shilnikov bifurcation

We now consider how the two-dimensional stable manifolds of the saddle-focus $p$ and saddle periodic orbits $\Gamma_k$ organize the overall dynamics in phase space near a chaotic Shilnikov bifurcation. Figure 9 shows the stable manifold $W^s(p)$ before and after the chaotic Shilnikov bifurcation for $\omega = -0.81$ in row (a) and $\omega = -0.83$ in row (b), respectively. Similar to before, the manifold has been computed as a one-parameter family of orbit segments, but now with fixed integration time $T_0 = 27$; see the Appendix for details. Both the solid rendering (left column) and the transparent rendering (right column) show the computed part of $W^s(p)$ as an intriguing bounded surface whose global geometry appears to be quite different from that observed near the simple Shilnikov bifurcation; in particular, the manifold $W^s(p)$ does not encompass the attracting equilibrium $q$; compare Fig. 9 with Figs. 3 and 4(b). The orbits of most points will end up at $q$ both before and after the chaotic Shilnikov bifurcation; due to the presence of the chaotic saddle $\mathcal{S}$ and depending on where they lie with respect to the different layers of $W^s(p)$, orbits may display complicated transient motion in the process.

Figure 10 shows a (blue) strip situated inside $W^s(p)$ (blue transparent surface) of orbit segments that follow (in backward time) the upper branch of $W^u(p)$ (red curve) back to a neighborhood of the saddle-focus $p$; more specifically, the computed orbit segments have begin points (in backward time) on the intersection $W_0$ of $W^s(p)$ with the sphere $S_R$ of radius $R = 0.3$ around $p$. The properties of the strip are illustrated further in Fig. 11, where it is shown in relation to $W^u(p)$ in panels (a)–(c) before, approximately at, and after the bifurcation, respectively. Notice the helicoidal nature of $W^s(p)$ in the enlargement panels (a2)–(c2); the only noticable difference through the bifurcation is again the fact that $W^u(p)$ lies on different sides of the strip before and after the bifurcation. Although the global structure of $W^s(p)$ is very different near the chaotic Shilnikov bifurcation, the properties of this strip of orbits in $W^s(p)$ that return to $S_R$ in backward time are effectively the same as those

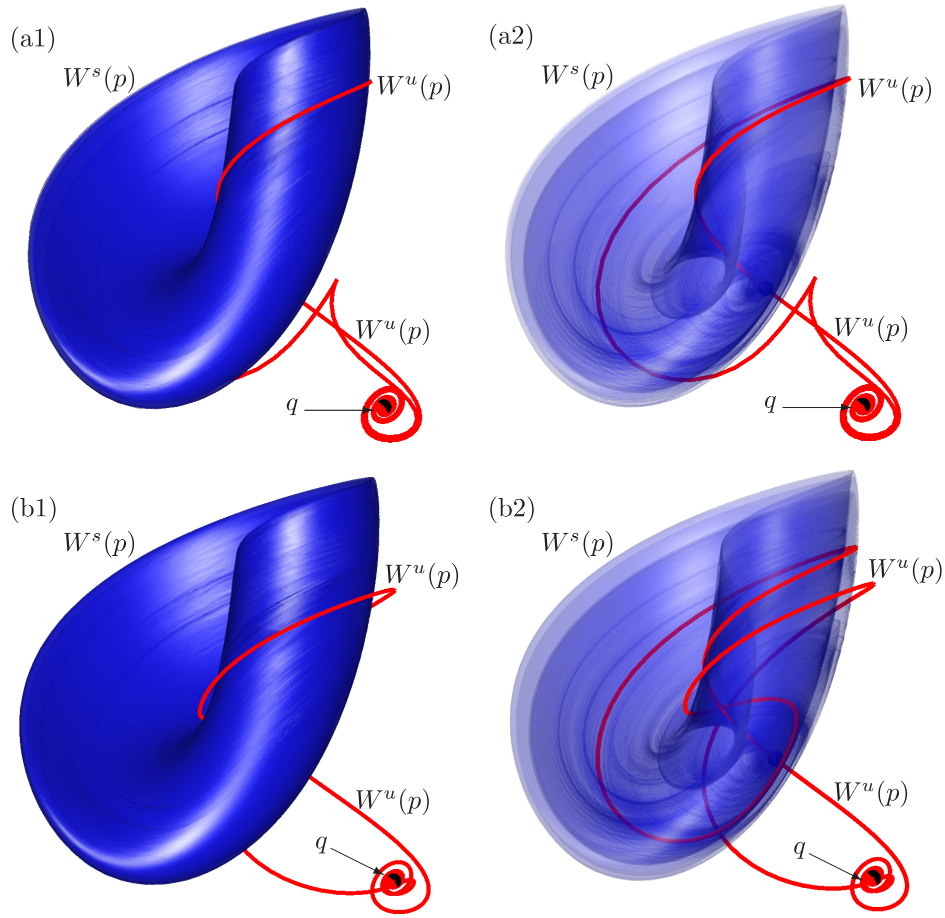


Figure 9: The two-dimensional stable manifold $W^s(p)$ (blue) before (row (a) for $\omega = -0.81$) and after (row (b) for $\omega = -0.83$) the chaotic Shilnikov homoclinic bifurcation in (4) for $k = 0.7$; also shown is $W^u(p)$ (red curve). The manifold $W^s(p)$ is represented by orbit segments of fixed integration time $T_0 = 27$; in the right panels it is rendered as a transparent surface.

of the corresponding strip near a simple Shilnikov bifurcation; compare Fig. 11(a1) and (c1) with Fig. 6(a1) and (b1), respectively. In other words, the first return (in backward time) of $W^s(p)$ to the sphere $S_R$ is very much the same near the two cases of a Shilnikov bifurcation.

### 4.1 Intersection of $W^s(p)$ with a sphere

What makes the chaotic Shilnikov bifurcation much more complicated is the fact that the manifold $W^s(p)$ returns to neighborhood of the saddle focus $p$ infinitely many times. In particular, for any sufficiently small sphere $S_R$ around $p$ and $\omega$ sufficiently close to $\omega_c^*$, the set $\widehat{W}^s(p) = W^s(p) \cap S_R$ consists of infinitely many

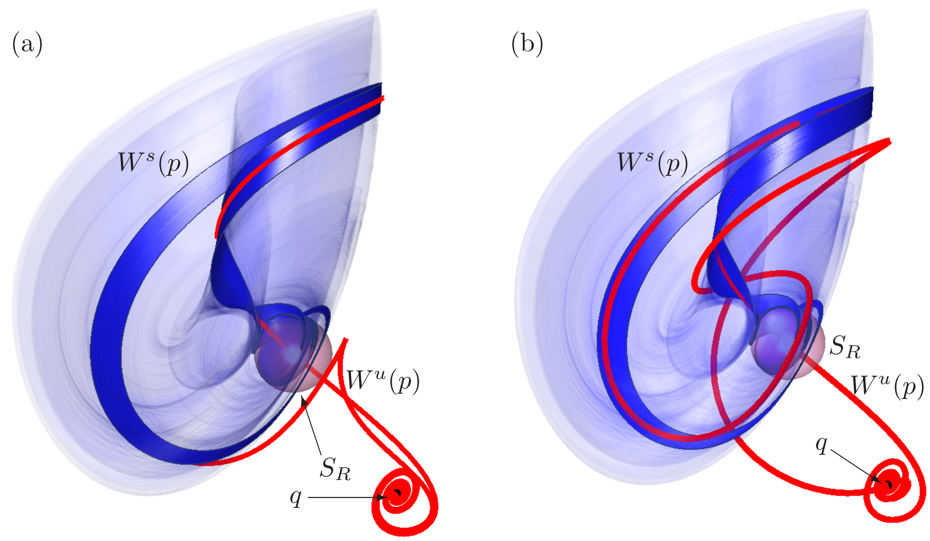


Figure 10: A (blue) strip of orbit segments inside $W^s(p)$ (blue transparent surface) as it returns to the sphere $S_R$ of radius $R = 0.3$ around the saddle-focus $p$, shown in panel (a) for $\omega = -0.81$ before, and panel (b) for $\omega = -0.83$ after the chaotic Shilnikov bifurcation in (4) for $k = 0.7$; also shown is $W^u(p)$ in red.

curves. We chose $R = 0.3$ in Figs. 10 and 11, so that the first two intersections curves are relatively easy to see, but this radius is too large to visualize properly the infinitely many intersection curves of $W^s(p)$ near the chaotic Shilnikov bifurcation; hence, we consider $S_R$ with a radius of $R = 0.055$ from now on and only plot its stereographic projection defined by (6). Figure 12 shows the set $\widehat{W}^s(p)$ of (blue) intersection curves of $W^s(p)$ and the (red) points of the set $\widehat{W}^u(p)$ on $S_R$, along with the tangency locus $C$. Figure 13 shows enlargements near $u_0 \in \widehat{W}^u(p)$ of the respective panels of Fig. 12. A special role is again played by the closed curve $W_0 = W^s_{\text{loc}}(p) \cap S_R$ that contains all other curves in $\widehat{W}^s(p)$ inside it. We further distinguish the curve $W_1 \in \widehat{W}^s(p)$ on which $u_0 \in \widehat{W}^u(p)$ lies at the primary Shilnikov bifurcation; both $W_0$ and $W_1$ are colored in a darker blue.

We now explain the geometry of this set before, at and after the chaotic Shilnikov bifurcation in more detail. For $\omega > \omega_c^*$, before the bifurcation, $\widehat{W}^s(p)$ is a nested set of infinitely many closed curves; see panels (a)–(d) of Fig. 12. We consider again the domain $\mathcal{D}$ that is bounded by the two darker blue curves $W_0$ and $W_1$ and contains $u_0 \in \widehat{W}^u(p)$ (red point). All other, infinitely many closed and nested curves in $\widehat{W}^s(p)$ lie in the domain $\mathcal{E}$ (shaded) that is bounded by $W_1$ only. Thus, orbits of points in $\mathcal{D}$ display the rather simple behavior of converging directly to the attracting equilibrium $q$. Orbits of points in $\mathcal{E}$, on the other hand, are more complicated and can make many excursions in phase space while following the many layers of $W^s(p)$; in particular, they may have many intersections with $S_R$ before ending up at $q$. As

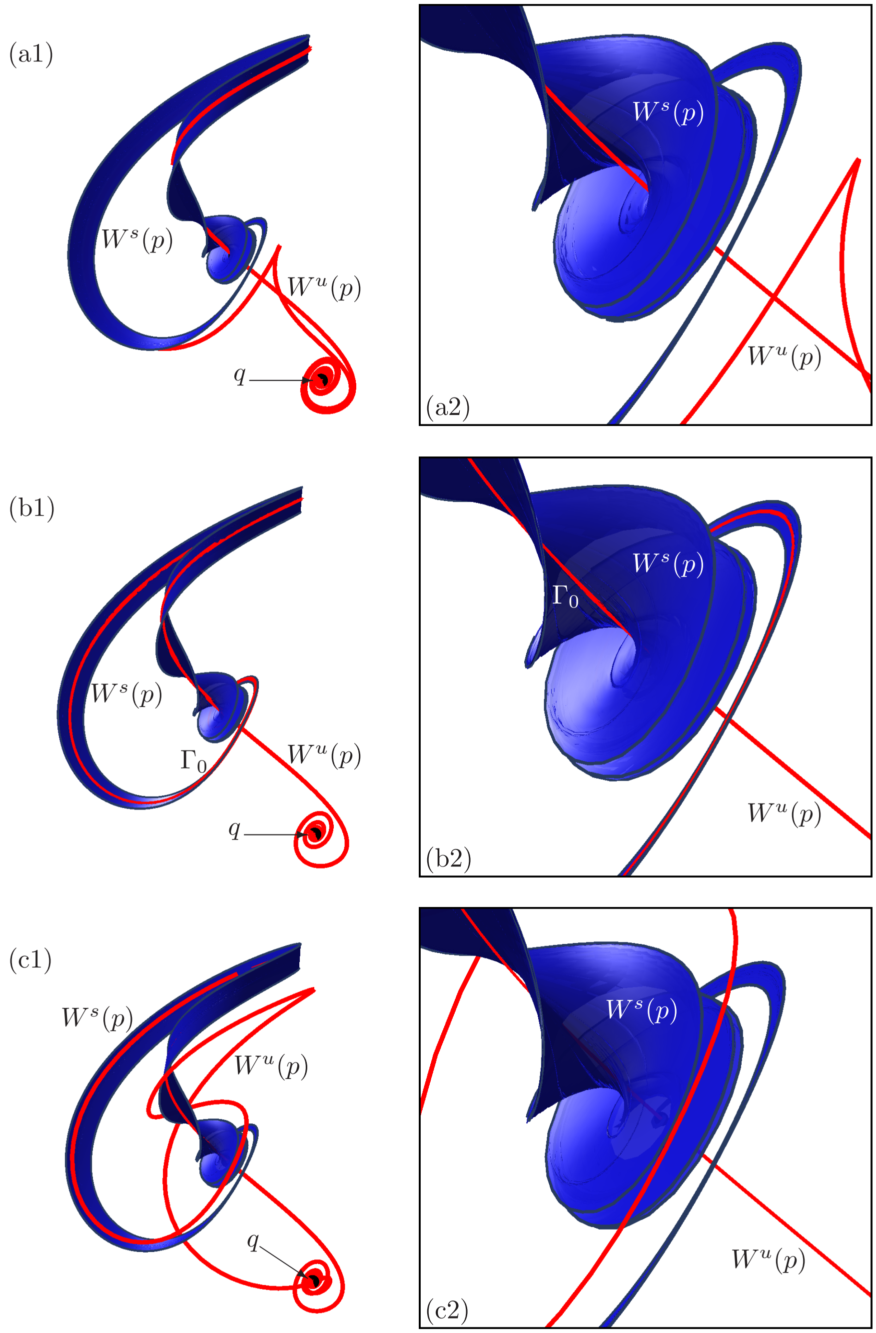


Figure 11: The (blue) strip of $W^s(p)$ before (row (a) for $\omega = -0.81$), approximately at (row (b) for $\omega = \omega_c^* \approx -0.820455$), and after (row (a) for $\omega = -0.83$) the chaotic Shilnikov bifurcation in (4) for $k = 0.7$, shown together with $W^u(p)$ (red curve); compare with Fig. 10.

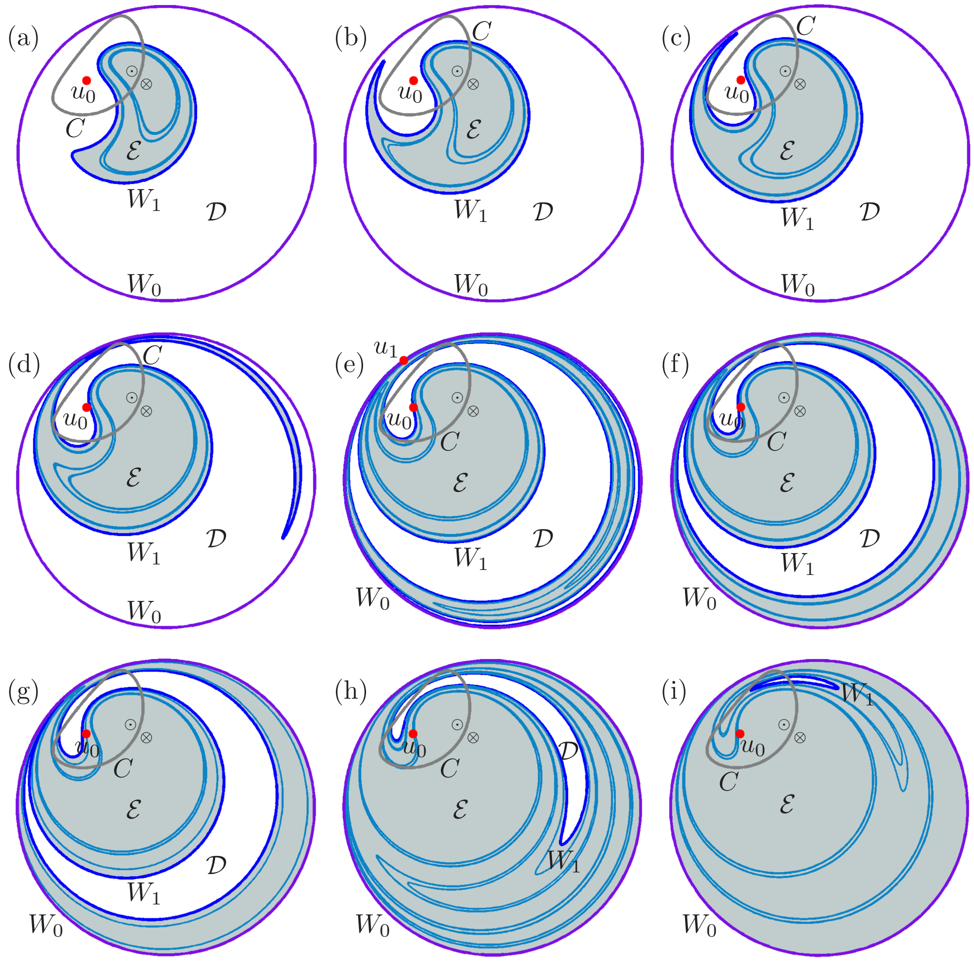


Figure 12: Stereographic projection of $\widehat{W}^s(p) = \{W_0, W_1, \ldots\}$ near a chaotic Shilnikov bifurcation. Panels (a)–(d) for $\omega \in \{-0.81, -0.813, -0.816, -0.818\}$ are before, panel (e) for $\omega = \omega_c^* \approx -0.820455$ is approximately at, and panels (f)–(i) for $\omega \in \{-0.822, -0.823, -0.827, -0.83\}$ are after the chaotic Shilnikov bifurcation in (4) for $k = 0.7$. The inside of the darker blue curve $W_0 = W^s_{\mathrm{loc}}(p) \cap S_R$ is divided into the two regions $\mathcal{D}$ and $\mathcal{E}$ (shaded) by the primary curve $W_1 \in \widehat{W}^s(p)$ (also colored in a darker blue); also shown are the (red) points $u_0, u_1 \in \widehat{W}^u(p)$.

was the case for the simple Shilnikov bifurcation, when the bifurcation value $\omega = \omega_c^*$ is approached, the domain $\mathcal{E}$ grows a 'tail' while the curve $W_1$ approaches $W_0$. At the bifurcation, $u_0 \in \widehat{W}^u(p)$ lies on the curve $W_1$; see panel (e) of Figs. 12 and 13. Moreover, $W_1$ is no longer a closed curve but an arc whose two ends accumulate on $W_0$. After the primary chaotic Shilnikov bifurcation, the domain $\mathcal{D}$ is bounded only by $W_1$ and the point $u_0$ lies in the domain $\mathcal{E}$, which is now bounded by both $W_1$ and $W_0$; see panels (f)–(i) of Fig. 12. We conclude that there is no difference between the two cases of Shilnikov bifurcation if one only considers the two curves

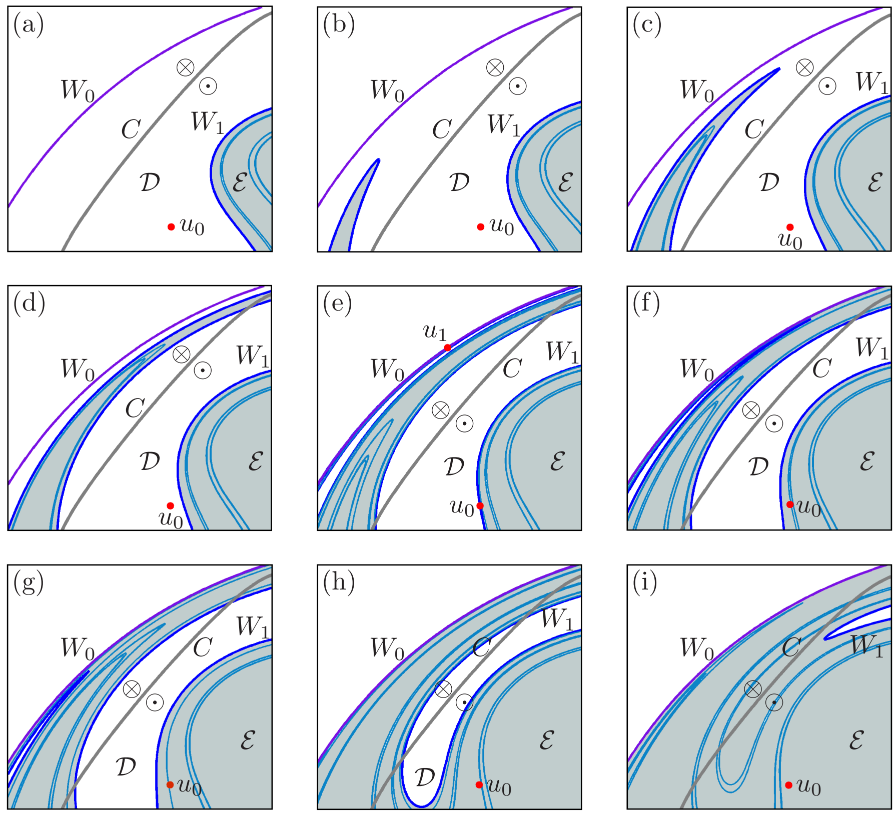


Figure 13: Enlargements near $u_0 \in \widehat{W}^u(p)$ of the respective panels of Fig. 12.

$W_0, W_1 \in \widehat{W}^s(p)$. More specifically, the curve $W_1$ undergoes the same topological transition via its accumulation on $W_0$.

The new feature of the chaotic Shilnikov bifurcation is the fact that there are now infinitely many closed curves of $\widehat{W}^s(p)$ that lie in the domain $\mathcal{E}$. After the bifurcation, the point $u_0 \in \widehat{W}^u(p)$ lies in $\mathcal{E}$ and, as the parameter $\omega$ is moved away from the bifurcation, it moves 'through' the other curves in $\widehat{W}^s(p)$. When $u_0 \in \widehat{W}^u(p)$ lies exactly on such a curve $W_l \subset \widehat{W}^s(p)$ then the upper branch of $W^u(p)$ lies in $W^s(p)$. Hence, there is a subsidiary Shilnikov bifurcation: an $n$-homoclinic orbit, where $W^u(p)$ returns to the saddle focus $p$ only at the $n$th return to a neighborhood of $p$ for some $n \geq 2$ (note that $n$ and $l$ need not be the same). Since the saddle quantity $\sigma = \sigma(\omega)$ is positive at $\omega_c^*$ and depends continuously on the parameter $\omega$, all subsidiary Shilnikov bifurcation are of the chaotic type, as long as $\sigma(\omega) > 0$. Figure 14 shows the situation before and after a subsidiary Shilnikov bifurcation due to the transitions of $u_0$ through a curve $W_l \in W^s(p)$. Notice that $W_l$ undergoes the same topological change — from closed curve, to arc accumulating on $W_0$, back to closed curve — that we found for the curve $W_1$ of the primary Shilnikov bifurcation.

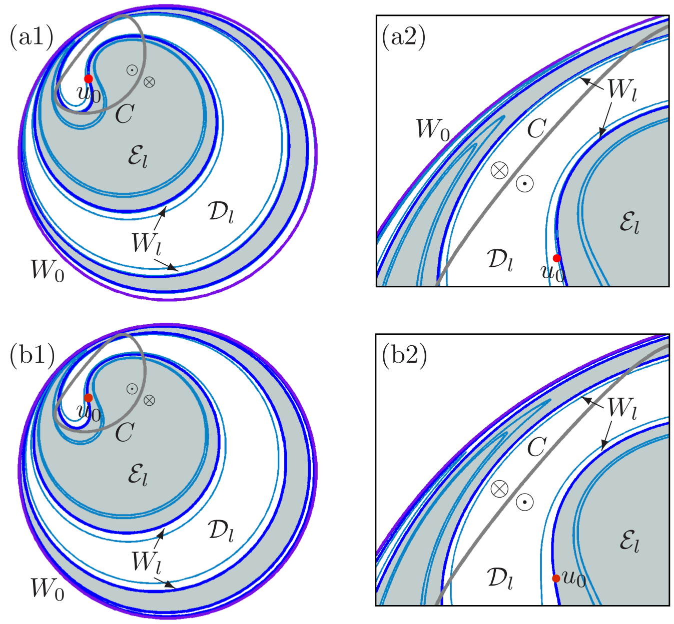


Figure 14: Stereographic projection of $\widehat{W}^s(p)$ before (row (a) for $\omega = -0.822$) and after (row (b) for $\omega = -0.823$) a subsidiary Shilnikov bifurcation associated with $u_0 \in \widehat{W}^u(p)$ crossing the darker blue curve $W_l \subset \widehat{W}^s(p)$; also shown are the corresponding domains $\mathcal{D}_l$ and $\mathcal{E}_l$ (shaded).

This is illustrated further in Fig. 14 by considering, as before, the corresponding sets $\mathcal{D}_l$ and $\mathcal{E}_l$ (shaded). Before the subsidiary Shilnikov bifurcation $\mathcal{D}_l$ is bounded by $W_0$ and $W_l$ and $\mathcal{E}_l$ is bounded by $W_l$ alone; see Fig. 14 (a). After the subsidiary Shilnikov bifurcation, on the other hand, $\mathcal{E}_l$ is bounded by both $W_0$ and $W_l$ and $\mathcal{D}_l$ is bounded by $W_l$ alone; see Fig. 14 (b).

In conclusion, we find an infinite sequence of subsidiary chaotic Shilnikov bifurcations after the primary chaotic Shilnikov bifurcation, each of which is associated with a particular closed curve $W_l \subset \widehat{W}^s(p)$ that undergoes the same topological change as the primary curve $W_1$. The fact that every subsidiary chaotic Shilnikov bifurcation unfolds just like the primary one explains the selfsimilar structure of the set $\widehat{W}^s(p)$. We remark that the sequence of topological changes of $\widehat{W}^s(p)$ near $\omega_c^*$ can be observed on $S_R$ provided that $R$ is sufficiently small. Moreover, the topological changes we find on the sphere $S_R$ are again not associated with interactions between the respective curves and the tangency locus $C$ on $S_R$. Hence, the topological changes of the set of curves $\widehat{W}^s(p)$ on $S_R$ represent global bifurcations of the two-dimensional manifold $W^s(p)$ in the three-dimensional phase space of (4).

## 4.2 The role of the saddle periodic orbits

The topological changes of $W^s(p)$ near $p$ through the primary chaotic Shilnikov homoclinic bifurcation and the subsequent $n$-homoclinic subsidiary Shilnikov bifurcations have been illustrated clearly in Figs. 12–14. However, the boundary of the basin $\mathcal{B}(q)$ is no longer formed by $W^s(p)$ alone; namely, one must take into account its interaction with the chaotic saddle $\mathcal{S}$ and the saddle periodic orbits $\{\Gamma_k\}_{k\in\mathbb{Z}}$ it contains. To keep this exposition simple, we concentrate here on the three representative and coexisting periodic orbits $\Gamma_{\mathbf{A}}$, $\Gamma_{\mathbf{B}}$ and $\Gamma_{\mathbf{C}}$ for $\omega = -0.83$ and $k = 0.7$ on the principal branch of periodic orbits shown in Fig. 1(b2). Note that this value of $\omega$ corresponds to the situation before the primary chaotic Shilnikov bifurcation.

Figure 15 shows the manifolds $W^s(\Gamma_{\mathbf{A}})$ (turquoise), $W^s(\Gamma_{\mathbf{B}})$ (cyan) and $W^s(\Gamma_{\mathbf{C}})$ (purple) from two different viewpoints in rows (a)–(c), respectively; note that the viewpoint in the left column is the same as that in Fig. 9. Each manifold is represented by a family of orbit segments (of fixed integration time $T_0 = 30$), computed with the method explained in the Appendix. The manifolds $W^s(\Gamma_{\mathbf{A}})$ and $W^s(\Gamma_{\mathbf{C}})$ are orientable (see the discussion in Section 1), which means that they consist of two sides separated by $\Gamma_{\mathbf{A}}$ and $\Gamma_{\mathbf{C}}$, respectively. One side of these manifolds is rendered as a solid surface in Figs. 15(a) and (c), while the other one is transparent. In contrast, the non-orientable manifold $W^s(\Gamma_{\mathbf{B}})$ is obtained by a single computation and shown as a solid surface in Fig. 15(b).

Note that the manifolds $W^s(p)$, $W^s(\Gamma_{\mathbf{A}})$, $W^s(\Gamma_{\mathbf{B}})$ and $W^s(\Gamma_{\mathbf{C}})$ have similar size and shape: they are all bounded and consist locally of a collection of layers; compare Figs. 9 and 15. In particular, since these are immersed manifolds, their boundedness implies a complicated structure in phase space. Figure 16 illustrates this further with the example of $\Gamma_{\mathbf{A}}$, the green period orbit with the lowest period of the three. Panel (a) shows only one side of the turqoise manifold $W^s(\Gamma_{\mathbf{A}})$ together with the blue manifold $W^s(p)$ to illustrate how close they are in phase space. More specifically, the side of $W^s(\Gamma_{\mathbf{A}})$ shown in Fig. 16 is the solid side from Fig. 15(a1), and $W^s(p)$ is as in Fig. 9(b2); the red unstable manifold $W^u(p)$ is included for reference. In fact, both sides of $W^s(\Gamma_{\mathbf{A}})$ lie entirely inside the region bounded by $W^s(p)$, and this turqoise manifold displays a very similar geometry. Panel (b) of Fig. 16(b) shows a strip of orbits in $W^s(\Gamma_{\mathbf{A}})$ that start on the sphere $S_R$ (not shown, but with $R = 0.3$ as in Fig. 9); by definition, these orbits approach the periodic orbit $\Gamma_{\mathbf{A}}$ in forward time, but they also come close to $p$ in backward time. Notice the characteristic helicoidal shape of $W^s(\Gamma_{\mathbf{A}})$ near the saddle focus $p$ and compare with $W^s(p)$ in Fig. 11.

## 4.3 Cantor structure of global stable manifolds

Figure 16 suggests that $W^s(\Gamma_{\mathbf{A}})$ must somehow lie 'in between' the layers of $W^s(p)$; the same applies to the other two manifolds $W^s(\Gamma_{\mathbf{B}})$ and $W^s(\Gamma_{\mathbf{C}})$. This gives a hint of the way these manifolds subdivide the phase space. We now consider in more detail the exact nature of this subdivision and the role of the chaotic saddle. To this end, we again consider the sets of intersection curves of these manifolds with the sphere $S_R$, where $R = 0.055$ as before.

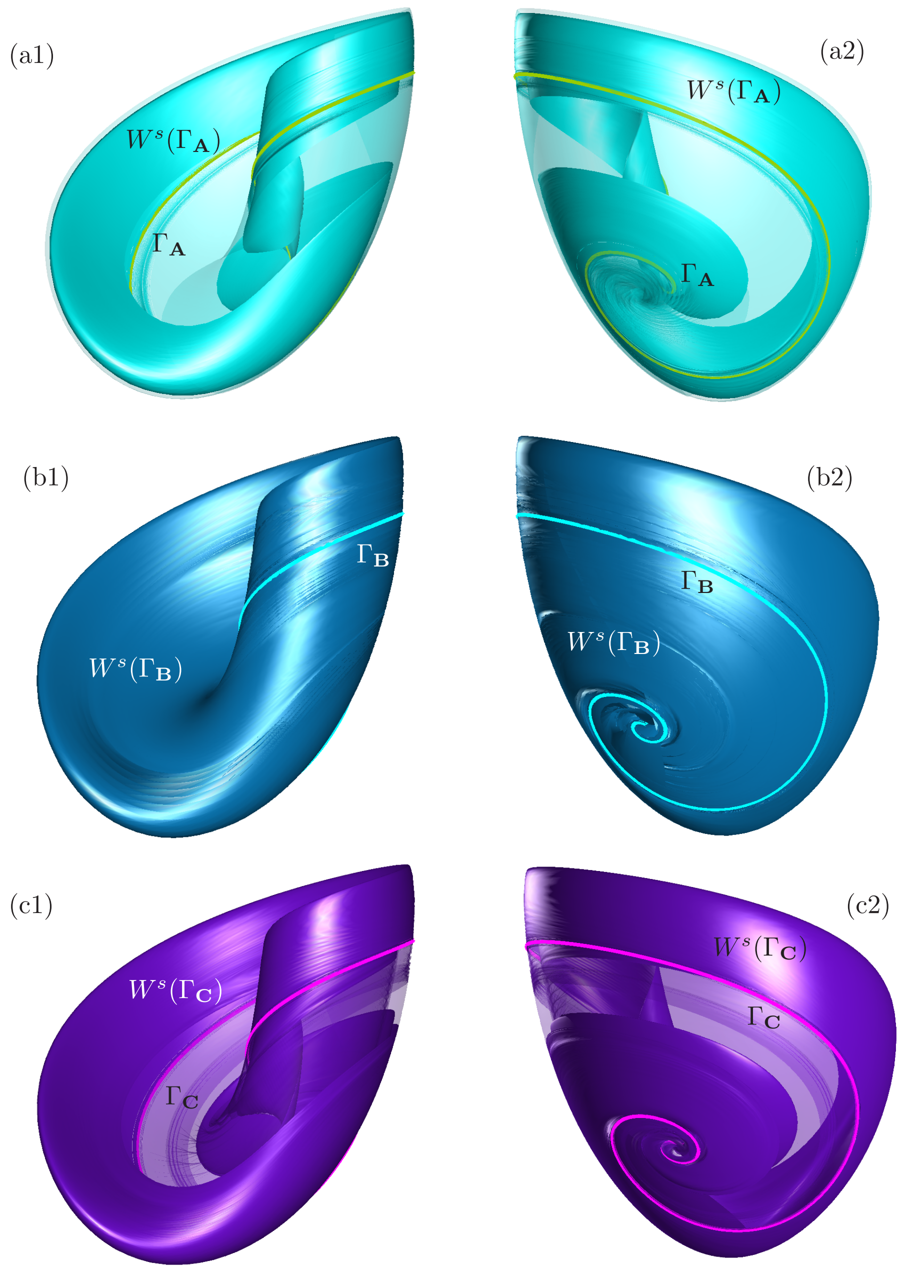


Figure 15: Two views each of the two-dimensional stable manifolds $W^s(\Gamma_{\mathbf{A}})$ (turquoise), $W^s(\Gamma_{\mathbf{B}})$ (cyan) and $W^s(\Gamma_{\mathbf{C}})$ (purple) of the coexisting saddle periodic orbits $\Gamma_{\mathbf{A}}$ (green), $\Gamma_{\mathbf{B}}$ (cyan) and $\Gamma_{\mathbf{C}}$ (magenta) for $\omega = -0.83$ and $k = 0.7$. The manifolds $W^s(\Gamma_{\mathbf{A}})$ and $W^s(\Gamma_{\mathbf{C}})$ are orientable; one side of them has been rendered transparent; $W^s(\Gamma_{\mathbf{B}})$ is non-orientable.

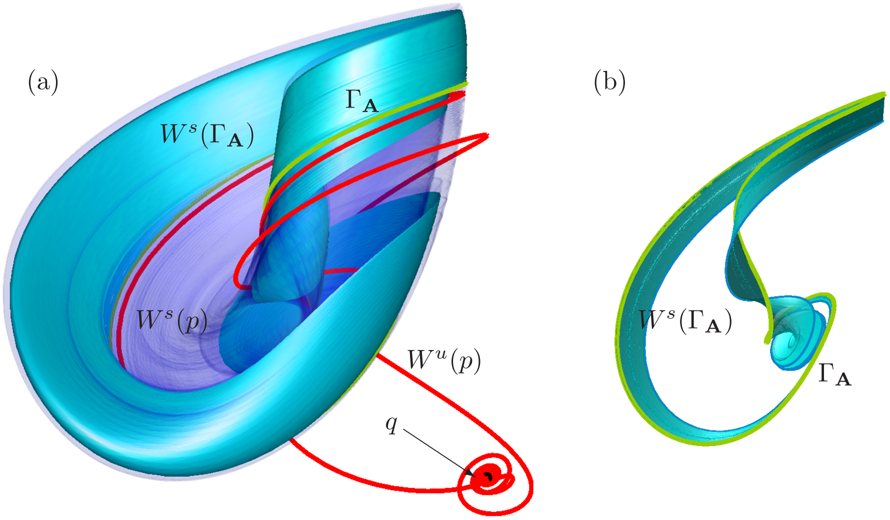


Figure 16: Panel (a) shows one side of the manifold $W^s(\Gamma_{\mathbf{A}})$ (turquoise) and the manifold $W^s(p)$ (transparent blue) for $\omega = -0.83$ and $k = 0.7$. Panel (b) shows a strip of orbit segments on $W^s(\Gamma_{\mathbf{A}})$ that return (in backward time) to a neighborhood of $p$.

Figure 17 shows in rows (a)–(c) the sets of computed intersection curves in $\widehat{W}^s(\Gamma_{\mathbf{A}}) := W^s(\Gamma_{\mathbf{A}}) \cap S_R$ (green), $\widehat{W}^s(\Gamma_{\mathbf{B}}) := W^s(\Gamma_{\mathbf{B}}) \cap S_R$ (cyan), and $\widehat{W}^s(\Gamma_{\mathbf{C}}) := W^s(\Gamma_{\mathbf{C}}) \cap S_R$ (magenta), approximately at the primary chaotic Shilnikov bifurcation for $\omega = \omega_c^* \approx -0.820455$. Also shown is the set $\widehat{W}^s(p)$ (blue curves). Here, we again show the stereographic projection (6) of $S_R$. For $\omega = \omega_c^*$, the sets $\widehat{W}^s(\Gamma_{\mathbf{A}})$, $\widehat{W}^s(\Gamma_{\mathbf{B}})$ and $\widehat{W}^s(\Gamma_{\mathbf{C}})$ consist of infinitely many disjoint, nested, closed curves that lie inside the region $\mathcal{E}$ whih is bounded by the curve $W_1 \subset \widehat{W}^s(p)$; compare with Figs. 12(e) and 13(e). Notice that the sets of curves in $\widehat{W}^s(\Gamma_{\mathbf{A}})$, $\widehat{W}^s(\Gamma_{\mathbf{B}})$ and $\widehat{W}^s(\Gamma_{\mathbf{C}})$ indeed lie in between the curves in $\widehat{W}^s(p)$, sharing their observed properties.

Suppose now that the parameter $\omega$ is changed past its value $\omega_c^*$ at the primary bifurcation, so that the point $u_0 \in \widehat{W}^u(p)$ enters the region $\mathcal{E}$ and crosses the curves in $\widehat{W}^s(\Gamma_{\mathbf{A}})$, $\widehat{W}^s(\Gamma_{\mathbf{B}})$ and $\widehat{W}^s(\Gamma_{\mathbf{C}})$. Every time $u_0$ lies on a curve in, say, $\widehat{W}^s(\Gamma_{\mathbf{A}})$ there is, hence, a codimension-one heteroclinic connection from the saddle focus equilibrium $p$ to the saddle periodic orbit $\Gamma_{\mathbf{A}}$; one also speaks of an EtoP connection [38]. Depending on which curve in $\widehat{W}^s(\Gamma_{\mathbf{A}})$ is involved, there will be a particular number of close approaches back to $p$ before $\Gamma_{\mathbf{A}}$ is reached. The transition through such an EtoP connection manifests itself topologically on $S_R$ in an already known way: before the EtoP connection the corresponding curve in $\widehat{W}^s(\Gamma_{\mathbf{A}})$ is one of the nested closed curves, at the bifurcation it is an arc whose two ends accumulate on $W_0$, and after the EtoP connection it is again closed.

Figure 18 shows all four sets of curves in $\widehat{W}^s(p)$ (blue), $\widehat{W}^s(\Gamma_{\mathbf{A}})$ (green), $\widehat{W}^s(\Gamma_{\mathbf{B}})$ (cyan), and $\widehat{W}^s(\Gamma_{\mathbf{C}})$ (magenta) in a single image. Indeed, it further illustrates that,

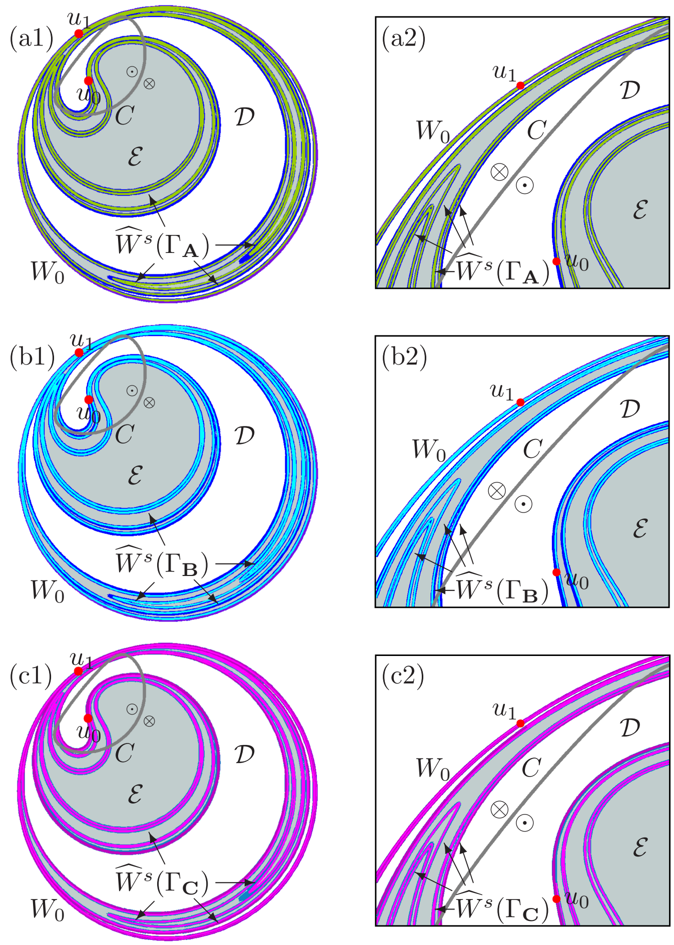


Figure 17: Stereographic projection of $\widehat{W}^s(p)$ together with $\widehat{W}^s(\Gamma_{\mathbf{A}})$ (green) in row (a), with $\widehat{W}^s(\Gamma_{\mathbf{B}})$ (cyan) in row (b), and with $\widehat{W}^s(\Gamma_{\mathbf{C}})$ (magenta) in row (c), shown for $\omega = \omega_c^* \approx -0.820455$ and $k = 0.7$; the right columns shows enlargements near $\{u_0, u_1\} \subset \widehat{W}^u(p)$ (red dots).

due to their boundedness, the different stable manifolds must lie very close to each other in phase space, as was already suggested by Figs. 15 and 16. Any intersection curve of a stable manifold lies in the complement of the basin $\widehat{\mathcal{B}}(q)$ of the attracting equilibrium $q$, which is identified in Fig. 18 as the white region. Notice that all intersection curves of stable manifolds lie in the region bounded by $W_0 \subset \widehat{W}^s(p)$. Furthermore, they are intricately intertwined in what appears to be the structure of a Cantor set of arcs.

To illustrate this further, we consider the horizontal line segment $L$ through the red point $u_0 \in \widehat{W}^u(p)$ in Fig. 18. Length and position of $L$ have been chosen in such a way that all curves in $\widehat{W}^s(p) \setminus \{W_0\}$, $\widehat{W}^s(\Gamma_{\mathbf{A}})$, $\widehat{W}^s(\Gamma_{\mathbf{B}})$ and $\widehat{W}^s(\Gamma_{\mathbf{C}})$ intersect $L$

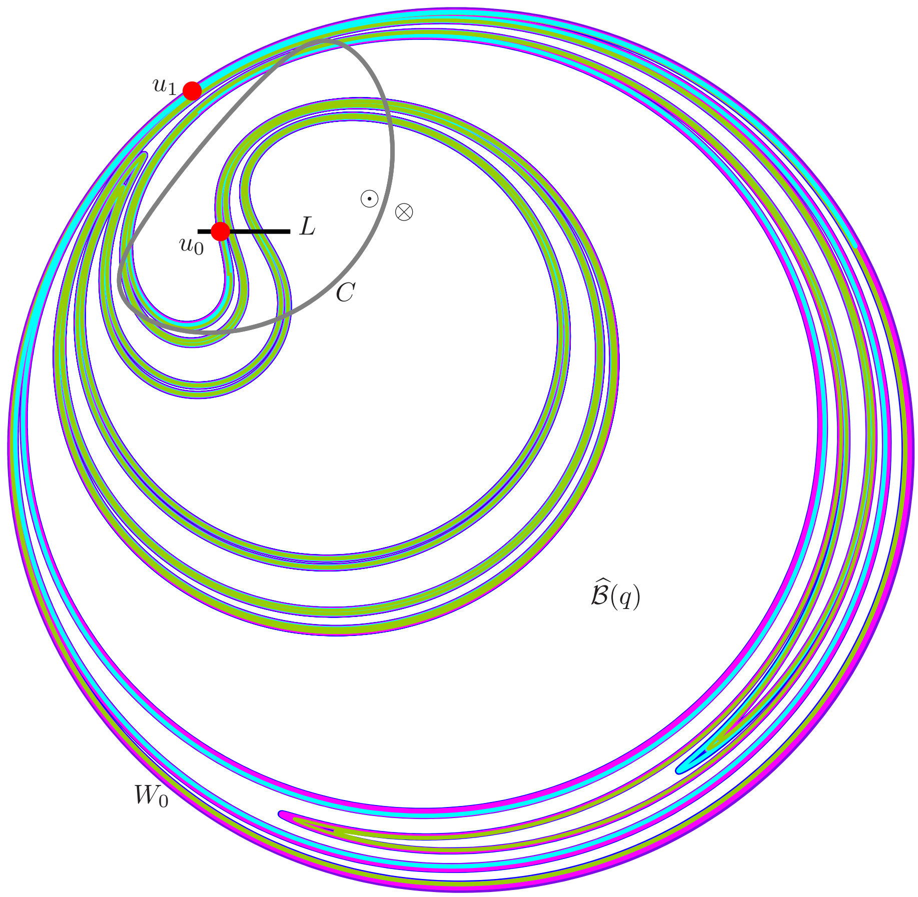


Figure 18: Stereographic projection of the four sets $\widehat{W}^s(p)$ (blue), $\widehat{W}^s(\Gamma_{\mathbf{A}})$ (green), $\widehat{W}^s(\Gamma_{\mathbf{B}})$ (cyan) and $\widehat{W}^s(\Gamma_{\mathbf{C}})$ (magenta) for $\omega = \omega_c^* \approx -0.820455$ and $k = 0.7$. These sets of global manifolds are subsets of $\widehat{W}^s(\mathcal{S})$, which is the complement in $S_R$ of the basin $\widehat{\mathcal{B}}(q)$.

exactly once and these intersections are transversal. Figure 19 shows a sequence of consecutive enlargements of the computed curves of stable manifolds near $L$, which clearly illustrates the underlying Cantor structure. More specifically, four clusters of curves can be identified in panel (a). Further enlargement reveals more details of the two leftmost and the two rightmost clusters in panel (b1) and (b2), respectively; panels (c1)–(c4) show the next level of enlargements in this process. While this is difficult to see in the figure, our numerical results show that each cluster of curves is bounded both on the left and on the right by a curve in $\widehat{W}^s(p)$.

From Figs. 17–19 the following general picture emerges. The observed Cantor structure of stable invariant manifolds is a manifestation in phase space of the chaotic saddle $\mathcal{S}$, which contains not only the saddle periodic orbits but also the saddle equilibrium $p$. More specifically, its stable manifold $W^s(\mathcal{S})$ is a compact set that

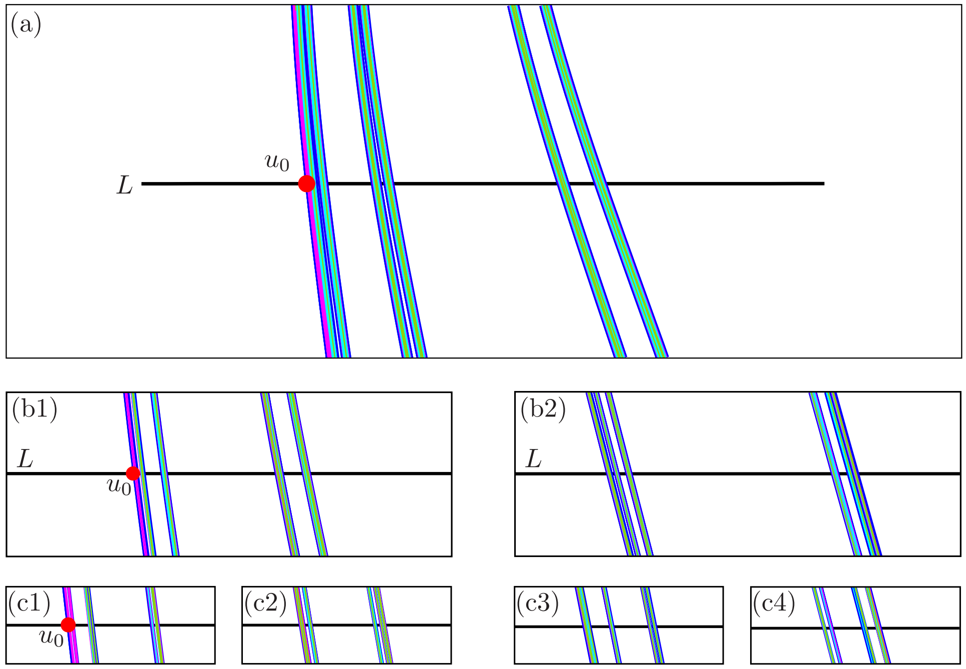


Figure 19: Successive enlargements of Fig. 18 near $L$, illustrating the Cantor structure of the intersection curves of stable manifolds on $S_R$.

contains $W^s(p)$, $W^s(\Gamma_{\mathbf{A}})$, $W^s(\Gamma_{\mathbf{B}})$ and $W^s(\Gamma_{\mathbf{C}})$, and forms the boundary of the basin $\mathcal{B}(q)$. The fact that the end points of the intervals in the complement of the Cantor set on the line segment $L$ in Fig. 19 are in $\widehat{W}^s(p) \cap L$ implies that $\overline{W^s(p)} = W^s(\mathcal{S})$, where $\overline{W^s(p)}$ is the closure of $W^s(p)$. Moreover, $W^s(p) \subset W^s(\mathcal{S})$ is the accessible boundary of the basin $\mathcal{B}(q)$.

Considering again the situation on the sphere $S_R$, the overall structure of the curves in $\widehat{W}^s(p)$, $\widehat{W}^s(\Gamma_{\mathbf{A}})$, $\widehat{W}^s(\Gamma_{\mathbf{B}})$ and $\widehat{W}^s(\Gamma_{\mathbf{C}})$ in Fig. 18 represents the intersection set $\widehat{W}^s(\mathcal{S}) := W^s(\mathcal{S}) \cap S_R$, which is the boundary of $\widehat{\mathcal{B}}(q)$. The curves of $\widehat{W}^s(\mathcal{S})$ separate the basin $\widehat{\mathcal{B}}(q)$ locally into large regions that coexist with arbitrarily thin strips of $\widehat{\mathcal{B}}(q)$. The orbit of an initial condition in such a thin strip is first approaching the chaotic saddle, spending a long time in a transient motion before finally converging to the attractor $q$ [27]. We argue that the time spent visiting the chaotic saddle depends on the width of the strip, which reflects 'how deep' it is in the Cantor structure. This feature of the saddle chaotic set has already been observed in other systems near homoclinic bifurcations — in particular, in the Lorenz equations where a chaotic saddle bifurcating from the first homoclinic bifurcation gives rise to the preturbulent regime [17, 32].

This brings us to the question of the global topological nature of the stable invariant manifolds on the sphere $S_R$. As we concluded in the discussion above, the local intersection of the set of curves $\widehat{W}^s(p)$ with any transverse line consists of the countably many points of a Cantor set that bound the open intervals in its complement. The (uncountable) Cantor set itself is the intersection of the set of curves $\widehat{W}^s(\mathcal{S})$ with said line. In particular, it follows that the set $\widehat{W}^s(p)$ and the intersection set $\widehat{W}^s(\Gamma_k) \subset \widehat{W}^s(\mathcal{S})$ of any saddle periodic orbit $\Gamma_k$ are locally disconnected. Moreover, the $\alpha$-limit set of $W^s(\Gamma_k)$ is $W^s(\mathcal{S})$, which implies that the set $\widehat{W}^s(\Gamma_k)$ accumulates on $\widehat{W}^s(\mathcal{S})$ and, hence, on $W^s(p)$. What is more, our computations indicate that the sets $\widehat{W}^s(\Gamma_{\mathbf{A}})$, $\widehat{W}^s(\Gamma_{\mathbf{B}})$ and $\widehat{W}^s(\Gamma_{\mathbf{C}})$ that we considered are dense in $\widehat{W}^s(\mathcal{S})$.

To summarize its properties, the set $\widehat{W}^s(\mathcal{S})$ on $S_R$ is closed, bounded, locally disconnected and locally homeomorphic to a Cantor bundle [29]. Moreover, $\widehat{W}^s(\mathcal{S})$ is connected, meaning that it cannot be partitioned into two nonempty subsets such that each subset has no points in common with the closure of the other. These properties identify $\widehat{W}^s(\mathcal{S})$ and, hence, the closure of $\widehat{W}^s(p)$, as an indecomposable continuum [33]. Note that indecomposable continua occur naturally in many (chaotic) dynamical systems as the closures of stable or unstable manifolds of planar diffeomorphisms. Concrete examples can be found in the Smale horseshoe map, the Hénon map and the Ikeda map; see [33, 51] for further details.

The global stable manifold $\overline{W^s(p)}$ in the three-dimensional phase space is compact. Therefore, also $W^s(\mathcal{S}) = \overline{W^s(p)}$ is an indecomposable continuum. In particular, it is locally homeomorphic to a Cantor set of discs. The stable manifold $W^s(p)$ of the saddle focus $p$, which is dense in $W^s(\mathcal{S})$, forms the accessible boundary of the basin $\mathcal{B}(q) \subset \mathbb{R}^3$. These topological properties formalize and are in agreement with the numerical observation that the two-dimensional manifolds $W^s(p)$, $W^s(\Gamma_{\mathbf{A}})$, $W^s(\Gamma_{\mathbf{B}})$ and $W^s(\Gamma_{\mathbf{C}})$ form a complicated collection of many interleaved layers in a bounded region of phase space. In spite of the complicated topology of its boundary, the basin $\mathcal{B}(q)$ is simply connected, that is, a topological sphere; this follows immediately from the fact that each point in $\mathcal{B}(q)$ is connected to $q$ by a unique forward trajectory of finite arclength.

To conclude this section we briefly discuss what happens as the parameter $\omega$ is changed through the primary chaotic Shilnikov bifurcation at $\omega_c^*$; let us denote the interval for this parameter variation by $\Omega_c$. Generically, the point $u_0 = u_0(\omega) \in \widehat{W}^u(p)$ follows a path $L = \{u_0(\omega) \; ; \; \omega \in \Omega_c\}$ transverse to the curves in $\widehat{W}^s(\mathcal{S})$, such as the line $L$ in Fig. 18. Under the assumption that $\omega$ parameterizes $L$, the Cantor set $\widehat{W}^s(\mathcal{S}) \cap L$ has a diffeomorphic image in $\Omega_c$. When $\omega$ is changed, it crosses this Cantor set in $\Omega_c$, which corresponds to topological changes of the indecomposable continuum $\widehat{W}^s(\mathcal{S})$ and, hence, the chaotic saddle $\mathcal{S}$ itself. Each open interval of $\widehat{\mathcal{B}}(q) \cap L$ corresponds to an open interval in $\Omega_c$ for which the indecomposable continuum is of the same topological type. On the other hand, two instances of $\widehat{W}^s(\mathcal{S})$ corresponding to $\omega$-values from different intervals, are not homeomorphic. Before the bifurcation, for $\omega < \omega_c^*$, the set $\widehat{W}^s(\mathcal{S})$ is a collection of infinitely many nested circles that are contained in the region $\mathcal{E}$, while $u_0(\omega) \in \mathcal{D}$. After the bifurcation, as the parameter $\omega$ is decreased from $\omega_c^*$, the point $u_0(\omega)$ enters $\mathcal{E}$. When $u_0(\omega)$ lies in the Cantor set $\widehat{W}^s(\mathcal{S}) \cap L$, a global bifurcation occurs (for example, an $n$-homoclinic orbit or an EtoP connection is encountered) and the corresponding curve in $\widehat{W}^s(\mathcal{S})$ that contains $u_0(\omega)$ is an arc whose two ends accumulate on $W_0 \in \widehat{W}^s(p)$; all other curves in $\widehat{W}^s(\mathcal{S})$ are closed curves.

As was the case in Sec. 3, the observations we made for the specific example of the laser model (4) appear to be an entirely general description of the topological properties of stable manifolds near any chaotic Shilnikov bifurcation. We summarize them as follows.

**Result 2** *(Chaotic Shilnikov bifurcation) Suppose that the parameter $\eta$ unfolds a chaotic Shilnikov bifurcation at $\eta = \eta_c^*$ of a saddle-focus $p$ of the vector field (1). Then, in a neighborhood of $\eta_c^*$ and on any sufficiently small sphere $S_R$ centered at $p$, the set $\widehat{W}^s(p) := W^s(p) \cap S_R$ consists of infinitely many curves. Its closure is the intersection set $\widehat{W}^s(\mathcal{S}) := W^s(\mathcal{S}) \cap S_R$ of the stable manifold of a chaotic saddle $\mathcal{S}$. The set $\widehat{W}^s(\mathcal{S})$ is an indecomposable continuum, and it contains as subsets the stable manifold $\widehat{W}^s(\Gamma_k)$ of any saddle periodic orbit $\Gamma_k$; the set $\widehat{W}^s(p) \subset \widehat{W}^s(\mathcal{S})$ is accessible from any point in $S_R$ outside a large enough neighborhood of $\widehat{W}^s(\mathcal{S})$. Furthermore, $W_0 := W^s_{\rm loc}(p) \cap S_R$ is always a closed curve that bounds $\widehat{W}^s(\mathcal{S})$ and the following holds:*

- *(C.1) For $\eta < \eta_c^*$ (before the bifurcation) there is a closed curve $W_1 \subset \widehat{W}^s(p)$ that bounds a simply connected region $\mathcal{E}$ that contains all curves in $\widehat{W}^s(\mathcal{S}) \setminus \{W_o, W_1\}$. As $\eta$ approaches $\eta_c^*$, the arclength of $W_1$ diverges.*

- *(C.2) For $\eta = \eta_c^*$ (at the bifurcation) the curve $W_1$ is an arc with infinite arclength, the two ends of which converge to the closed curve $W_0$.*

- *(C.3) For $\eta > \eta_s^*$ (after the bifurcation) $W_1$ is again a closed curve with finite arclength and the region $\mathcal{E}$ is bounded by both $W_0$ and $W_1$. There is a Cantor set of parameter values at which $\widehat{W}^s(\mathcal{S})$ changes topologically. In particular, whenever the intersection point $u_0 \in \widehat{W}^u(p)$ crosses a curve in $\widehat{W}^s(p)$, there is a subsidiary chaotic Shilnikov bifurcation of an $n$-homoclinic orbit with $n \geq 2$. Similarly, there is an EtoP heteroclinic connection of codimension one whenever the intersection point $u_0$ crosses a curve in $\widehat{W}^s(\Gamma_k)$. At each such global bifurcation the intersection curve of the associated global manifold changes topologically in the same way as $W_1$ does at the primary Shilnikov bifurcation.*

# 5 Discussion

We have analyzed the role of two-dimensional global invariant manifolds in the transition through a Shilnikov homoclinic bifurcation of a saddle focus equilibrium $p$ of a three-dimensional vector field; as a specific example we considered model equations for an optically injected laser. We identified two points of simple and chaotic Shilnikov bifurcation on a curve of primary homoclinic bifurcations, respectively, and then varied the single parameter $\omega$ to study the transition through the respective codimension-one bifurcation.

We employed a boundary value problem setup to compute the two-dimensional stable manifolds $W^s(p)$ of $p$ and $W^s(\Gamma_k)$ of bifurcating saddle periodic orbits $\Gamma_k$; moreover, this setup also allows one to compute the sets of intersection curves of these manifolds with suitably chosen surfaces in phase space. In this way, we demonstrated that all information on the topological changes associated with the Shilnikov bifurcation can be represented comprehensively by considering the intersection curves of the two-dimensional stable manifolds with a sufficiently small sphere $S_R$ around $p$. The topological properties of the stable manifolds that we found for the laser model appear to be generic and, hence, are expected to be found near any simple or chaotic Shilnikov bifurcation.

For the case of a simple Shilnikov bifurcation, where a single stable periodic orbit $\Gamma$ bifurcates from the homoclinic orbit, there are exactly two intersection curves, $W_0$ and $W_1$, of $W^s(p)$ with a sphere $S_R$ centered at $p$, provided its radius $R$ is small enough. As the bifurcation is approached, the closed curve $W_1$ starts to 'wind up' on the closed curve $W_0$, which is the intersection of $W^s_{\text{loc}}(p)$ with $S_R$. At the bifurcation, the curve $W_1$ contains a point $u_0 \in W^u(p)$ and it is an arc whose two ends accumulate on $W_0$. After the bifurcation, $W_1$ is again a closed curve that 'unwinds' from $W_0$ as the parameter is moved further away from the bifurcation value. Effectively, in this bifurcation, the regions bounded by $W_0$ and $W_1$ turn 'inside-out,' and one of them becomes the basin of the bifurcating attracting periodic orbit $\Gamma$.

For the case of a chaotic Shilnikov bifurcation, on the other hand, the stable manifold $W^s(p)$ intersects the sphere $S_R$ not only in the two curves $W_0$ and $W_1$, but in infinitely many other curves, which all lie inside the same region of $S_R$ bounded by $W_0$. Moreover, before the bifurcation these additional intersection curves all lie in the region bounded by $W_1$. At the bifurcation $W_1$ undergoes exactly the same topological transition as we found for the simple Shilnikov bifurcation. However, this means now that the point $u_0 \in W^u(p) \cap S_R$ enters the region with infinitely many additional intesection curves of $W^s(p)$ and $S_R$. As a consequence, we find a subsidiary chaotic Shilnikov bifurcation whenever $u_0 \in W^u(p) \cap S_R$ crosses one of these additional curves, which then also 'winds up' and 'unwinds' onto $W_0$ exactly as $W_1$ did. What is more, we showed with three examples how the two-dimensional stable manifolds $W^s(\Gamma_k)$ of saddle periodic orbits $\Gamma_k$ intersect the sphere $S_R$ in a very similar fashion, giving rise to infinitely many codimension-one heteroclinic bifurcations between $p$ and $\Gamma_k$ as the parameter is varied past the primary chaotic Shilnikov bifurcation.

Our investigations show for the chaotic Shilnikov bifurcation that the closure of $W^s(p)$ is the stable manifold $W^s(\mathcal{S})$ of a chaotic saddle $\mathcal{S}$ that exist in a tubular neighborhood of the primary homoclinic orbit. The set $W^s(\mathcal{S})$ also contains the manifolds $W^s(\Gamma_k)$ of the saddle periodic orbits, and its intersection with $S_R$ is an indecomposable continuum that is locally a Cantor bundle of arcs. Moreover, the manifold $W^s(p)$ is in the accessible boundary of the complement in phase space of the tubular neighborhood containing $\mathcal{S}$. When the unfolding parameter is varied past the primary chaotic Shilnikov bifurcation one encounters uncountably many topological changes of the indecomposable continuum at a Cantor set of parameter values; in particular, there are infinitely many subsidiary chaotic Shilnikov bifurcations of $n$-

homoclinic orbits and infinitely many codimension-one heteroclinic (EtoP) orbits between $p$ and the periodic orbits $\Gamma_k$. Note that there are other bifurcations (which we did not consider here) that change the chaotic saddle $\mathcal{S}$. In particular, near the primary and near all subsidiary chaotic Shilikov bifurcations one finds infinitely many saddle-node bifurcations of periodic orbits; the bifurcating periodic orbits of saddle type are subsets of $\mathcal{S}$, and they may undergo further bifurcations, including period-doubling and torus bifurcations.

We remark that the overall topological structure of the two-dimensional stable manifolds near the chaotic Shilnikov bifurcation is different from that which one finds due to the existence of a chaotic saddle near other global bifurcations. For instance, after the homoclinic explosion in the Lorenz system one also finds an indecomposable continuum on a suitable sphere, but it has very different properties [17]. More specifically, it is the closure of the intersection curves with the sphere of the two-dimensional stable manifolds of the pair of saddle periodic orbits that bifurcated from the main homoclinic bifurcation (also known as the homoclinic explosion point). The stable manifold of the origin (the saddle equilibrium of the system), on the other hand, is locally connected and a separatrix between the basins of two (symmetrically related) attracting equilibria; see [17] for more details.

The numerical setup that we used in this work can also be employed for the study of the role of (un)stable manifolds in other global bifurcations. In ongoing work we are analyzing the nature of the stable manifold of a saddle with real eigenvalues near codimension-two homoclinic flip bifurcation points [30, 46], which are key for understanding transitions between orientable and non-orientable manifolds. This is an example of a global bifurcation of codimension two; other examples of codimension-two bifurcations near which manifold computations may provide global insight include non-central saddle-node homoclinic points [58, 61] or Belyakov points [6].

## References


[1] P. Aguirre, E. Doedel, B. Krauskopf and H. M. Osinga, *Investigating the consequences of global bifurcations for two-dimensional manifolds of vector fields*, DCDS-A, **29** (2011), 1309–1344.

[2] P. Aguirre, E. González-Olivares and E. Sáez, *Three limit cycles in a Leslie-Gower predator-prey model with additive Allee effect*, SIAM J. Appl. Math., **69** (2009), 1244–1262.

[3] R. Barrio, F. Blesa and S. Serrano, *Qualitative analysis of the Rössler equations: Bifurcations of limit cycles and chaotic attractors*, Physica D, **238** (2009), 1087–1100.

[4] M. R. Bassett and J. L. Hudson, *Shil'nikov chaos during copper electrodissolution*, J. Phys. Chem., **92** (1988), 6963–6966.

[5] L. A. Belyakov, *A case of the generation of a periodic motion with homoclinic curves*, Mat. Zam., **15** (1974), 571–580.

[6] L. A. Belyakov, *Bifurcation of systems with homoclinic curve of a saddle-focus with saddle quantity zero*, Mat. Zam., **36** (1984), 681–689.

[7] W. J. Beyn, *On well-posed problems for connecting orbits in dynamical systems*, in "Chaotic Numerics" (Geelong, 1993), Contemp. Math., Vol. 172, Amer. Math. Soc., (1994), 131–168.

[8] A. R. Champneys, V. Kirk, E. Knobloch, B. E. Oldeman and J. Sneyd, *When Shil'nikov meets Hopf in excitable systems*, SIAM J. Appl. Dyn. Syst., **6** (2007), 663–693.

[9] A. R. Champneys, Y. Kuznetsov and B. Sandstede, *A numerical toolbox for homoclinic bifurcation analysis*, Int. J. Bifurc. Chaos, **6** (1996), 867–887.

[10] M. G. Clerc, P. C. Encina and E. Tirapegui, *Shilnikov bifurcation: stationary quasi-reversal bifurcation*, Int. J. Bifurc. Chaos, **18** (2008), 1905–1915.

[11] B. Deng and G. Hines, *Food chain chaos due to Shilnikov's orbit*, Chaos, **12** (2002), 533–538.

[12] M. Desroches, B. Krauskopf and H. M. Osinga, *The geometry of slow manifolds near a folded node*, SIAM J. Appl. Dyn. Syst., **7** (2008), 712–754.

[13] A. Dhooge, W. Govaerts and Yu. A. Kuznetsov, *MATCONT: A Matlab package for numerical bifurcation analysis of ODEs*, ACM Trans. Math. Software, **29** (2003), 141–164.

[14] E. J. Doedel, *AUTO: A program for the automatic bifurcation analysis of autonomous systems*, Congr. Numer., **30** (1981), 265–284.

[15] E. J. Doedel, *Lecture notes on numerical analysis of nonlinear equations,* in "Numerical Continuation Methods for Dynamical Systems" (eds. B. Krauskopf, H. M. Osinga and J. Galán-Vioque), Underst. Complex Syst., Springer-Verlag, New York, (2007), 1–49.

[16] E. J. Doedel, B. Krauskopf and H. M. Osinga, *Global bifurcations of the Lorenz manifold*, Nonlinearity, **19** (2006), 2947–2972.

[17] E. J. Doedel, B. Krauskopf and H. M. Osinga, *Global invariant manifolds in the transition to preturbulence in the Lorenz system*, submitted to Indagationes Mathematicae. Pre-print available at `http://hdl.handle.net/1983/1743`.

[18] E. J. Doedel and B. E. Oldeman with major contributions from A. R. Champneys, F. Dercole, T. F. Fairgrieve, Y. Kuznetsov, R. C. Paffenroth, B. Sandstede, X. J. Wang and C. H. Zhang, *AUTO-07p Version 0.7: Continuation and bifurcation software for ordinary differential equations*, Department of Computer Science, Concordia University, Montreal, Canada, (2010). Available from `http://cmvl.cs.concordia.ca/`.

[19] J. P. England, B. Krauskopf and H. M. Osinga, *Computing one-dimensional global manifolds of Poincaré maps by continuation*, SIAM J. Appl. Dyn. Sys., **4** (2005), 1008–1041.

[20] J. P. England, B. Krauskopf and H. M. Osinga *Computing two-dimensional global invariant manifolds in slow-fast systems*, Internat. J. Bifur. Chaos Appl. Sci. Engrg., **17** (2007), 805–822.

[21] J. A. Feroe, *Homoclinic orbits in a parametrized saddle-focus system*, Physica D, **62** (1993), 254–262.

[22] M. Friedman and E. J. Doedel, *Numerical computation and continuation of invariant manifolds connecting fixed points*, SIAM J. Numer. Anal., **28** (1991), 789–808.

[23] P. Gaspard, R. Kapral and G. Nicolis, *Bifurcation phenomena near homoclinic systems: A two-parameter analysis*, J. Statist. Phys., **35** (1984), 697–727.

[24] P. Glendinning and C. Sparrow, *Local and global behavior near homoclinic orbits*, J. Statist. Phys., **35** (1984), 645–696.

[25] G. Gómez, W. S. Koon, M. W. Lo, J. E. Marsden, J. Masdemont and S. D. Ross, *Invariant manifolds, the spatial three-body problem and space mission design*, Astrodynamics Specialist Meeting, Quebec City, Canada, (2001), AAS 01-31.

[26] W. Govaerts and Y. A. Kuznetsov, *Interactive continuation tools*, in "Numerical Continuation Methods for Dynamical Systems," (eds. B. Krauskopf, H. M. Osinga and J. Galán-Vioque), Underst. Complex Syst., Springer-Verlag, New York, (2007), 51–75.

[27] J. Guckenheimer and P. Holmes, "Nonlinear Oscillations, Dynamical Systems and Bifurcations of Vector Fields," $2^{nd}$ edition, Springer-Verlag, New York/Berlin, 1986.

[28] J. Guckenheimer and C. Kuehn, *Homoclinic orbits of the FitzHugh-Nagumo equation: Bifurcations in the full system*, SIAM J. Appl. Dyn. Syst., **9** (2010), 138–152.

[29] A. Gutek and J. van Mill, *Continua that are locally a bundle of arcs*, Topology Proceedings, **7** (1982), 63–69.

[30] A. J. Homburg and B. Krauskopf, *Resonant homoclinic flip bifurcations*, J. Dynam. Diff. Eqs., **12** (2000), 807–850.

[31] F. C. Hoppensteadt, "An Introduction to the Mathematics of Neurons, Modeling in the Frequency Domain," Cambridge University Press, Cambridge, 1997.

[32] E. A. Jackson, *The Lorenz system: II. The homoclinic convolution of the stable manifolds*, Phys. Scr., **32** (1985), 469–475.

[33] J. Kennedy, *How indecomposable continua arise in dynamical systems*, Annals of the New York Academy of Sciences, **704** (1993), 180–201.

[34] B. Krauskopf and H. M. Osinga, *Two-dimensional global manifolds of vector fields*, Chaos, **9** (1999), 768–774.

[35] B. Krauskopf and H. M. Osinga, *Computing geodesic level sets on global (un)stable manifolds of vector fields*, SIAM J. Appl. Dyn. Sys., **2** (2003), 546–569.

[36] B. Krauskopf and H. M. Osinga, *Computing invariant manifolds via the continuation of orbit segments*, in "Numerical Continuation Methods for Dynamical Systems," (eds. B. Krauskopf, H. M. Osinga and J. Galán-Vioque), Underst. Complex Syst., Springer-Verlag, New York, (2007), 117–154.

[37] B. Krauskopf, H. M. Osinga, E. J. Doedel, M. E. Henderson, J. Guckenheimer, A. Vladimirsky, M. Dellnitz and O. Junge, *A survey of methods for computing (un)stable manifolds of vector fields*, Internat. J. Bifur. Chaos Appl. Sci. Engrg., **15** (2005), 763–791.

[38] B. Krauskopf and T. Riess, *A Lin's method approach to finding and continuing heteroclinic orbits connections involving periodic orbits*, Nonlinearity, **21** (2008), 1655–1690.

[39] B. Krauskopf, K. Schneider, J. Sieber, S. Wieczorek and M. Wolfrum, *Excitability and self-pulsations near homoclinic bifurcations in semiconductor lasers*, Optics Communications, **215** (2003), 230–249.

[40] Yu. A. Kuznetsov, "Elements of Applied Bifurcation Theory," $3^{rd}$ edition, Springer-Verlag, New York/Berlin, 2004.

[41] C. M. Lee, P. J. Collins, B. Krauskopf and H. M. Osinga, *Tangency bifurcations of global Poincaré maps*, SIAM J. Appl. Dyn. Syst., **7** (2008), 712–754.

[42] E. N. Lorenz, *Deterministic nonperiodic flows*, J. Atmosph. Sci., **20** (1963), 130–141.

[43] J. R. Munkres, "Topology", $2^{nd}$ edition, Prentice Hall, Upper Saddle River, NJ, 2000.

[44] T. Noh, *Shilnikov's chaos in the oxidation of formic acid with bismuth ion on Pt ring electrode*, Electrochimica Acta, **54** (2009), 3657–3661.

[45] B. E. Oldeman, A. R. Champneys and B. Krauskopf, *Homoclinic branch switching: a numerical implementation of Lin's method*, Internat. J. Bifur. Chaos Appl. Sci. Engrg., **13** (2003), 2977–2999.

[46] B. E. Oldeman, B. Krauskopf and A. R. Champneys, *Numerical unfoldings of codimension-three resonant homoclinic flip bifurcations*, Nonlinearity, **14** (2001), 597–621.

[47] H. M. Osinga, *Nonorientable manifolds in three-dimensional vector fields*, Internat. J. Bifur. Chaos, **13** (2003), 553–570.

[48] I. M. Ovsyannikov and L. P. Shil'nikov, *On systems with a saddle-focus homoclinic curve*, Math. USSR Sbornik, **58** (1987), 557–574.

[49] T. Peacock and T. Mullin, *Homoclinic bifurcations in a liquid crystal flow*, J. Fluid Mech., **432** (2001), 369-386.

[50] A. M. Rucklidge, *Chaos in a low-order model of magnetoconvection*, Physica D, **62** (1993), 323–337.

[51] M. A. F. Sanjuán, J. Kennedy, E. Ott and J. A. Yorke, *Indecomposable continua and the characterization of strange sets in nonlinear dynamics*, Phys. Rev. Lett., **78** (1997), 1892–1895.

[52] L. P. Shilnikov, *A case of the existence of a countable number of periodic orbits*, Sov. Math. Dokl., **6** (1965), 163–166.

[53] L. P. Shilnikov, *A contribution to the problem of the structure of an extended neighborhood of a rough state to a saddle-focus type*, Math. USSR-Sb, **10** (1970), 91–102.

[54] L. P. Shilnikov, A. L. Shilnikov, D. V. Turaev and L. Chua, "Methods of Qualitative Theory in Nonlinear Dynamics, Part II," World Scientific Series on Nonlinear Science, Series A, Vol. 5, 2001.

[55] S. H. Strogatz, "Nonlinear Dynamics and Chaos: With Applications to Physics, Biology, Chemistry and Engineering," Adison-Wesley, Reading, MA, 1994.

[56] G. A. K. van Voorn, B. W. Kooi and M. P. Boer, *Ecological consequences of global bifurcations in some food chain models*, Math. Biosc., **226** (2010), 120–133.

[57] K. Watada, T. Endo and H. Seishi, *Shilnikov orbits in an autonomous third-order chaotic phase-locked loop*, IEEE Trans. on Circ. and Syst. I, **45** (1998), 979–983.

[58] S. Wieczorek and B. Krauskopf, *Bifurcations of $n-$homoclinic orbits in optically injected lasers*, Nonlinearity, **18** (2005), 1095–1120.

[59] S. Wieczorek, B. Krauskopf and D. Lenstra, *A unifying view of bifurcations in a semiconductor laser subject to optical injection*, Optics Communications, **172** (1999), 279–295.

[60] S. Wieczorek, B. Krauskopf and D. Lenstra, *Multipulse excitability in a semiconductor laser with optical injection*, Physical Review Letters, **88** (2002), 1–4.

[61] S. M. Wieczorek, B. Krauskopf, T. B. Simpson, and D. Lenstra, *The dynamical complexity of optically injected semiconductor lasers*, Phys. Reports, **416** (2005), 1–128.

[62] S. Wiggins, "Introduction to Applied Nonlinear Dynamical Systems and Chaos," $2^{nd}$ edition, Springer-Verlag, New York/Berlin, 2003.

## Appendix: Computation of global invariant manifolds

In general, there are no analytical expressions for homoclinic orbits and associated global (un)stable manifolds. Therefore, one must use numerical techniques to obtain them. Homoclinic and heteroclinic orbits can readily be computed with continuation software packages such as AUTO [14, 18] and MATCONT [13, 26]. We used HOMCONT [9], which is a standard extension of AUTO for the detection and continuation of connecting orbits based on projection boundary conditions [7]; see also [22, 45, 46]. Here, we describe the numerical techniques used to compute the two-dimensional global stable manifolds of the equilibrium and periodic orbits in this paper. Precise details can be found, for example, in the survey papers [36, 37].

A two-dimensional invariant manifold of a vector field can be thought of as a one-parameter family of orbits. Hence, any finite part of interest of such a manifold can be computed as a family of finite-time orbit segments that are solutions of a suitable two-point boundary value problem (BVP). We make use of the boundary value solver of AUTO to find such a family of orbit segments by continuation [15, 36]. The general set-up in AUTO, assuming that the vector field is three-dimensional, is to consider a function

$$\mathbf{u} : [0, 1] \mapsto \mathbb{R}^3$$

that satisfies the differential equation

$$\dot{\mathbf{u}} = T f(\mathbf{u}(t)) \tag{8}$$

Equation (8) is the scaled form of the vector field defined by $f$. Any solution $\mathbf{u}$ of (8) defined on the time interval $[0, 1]$ corresponds to a solution $\mathbf{x} : [0, T] \mapsto \mathbb{R}^3$, with $T > 0$, of the unscaled vector field via the transformation $\mathbf{x}(t) = \mathbf{u}(t/T)$, with $0 \leq t \leq T$. The total integration time $T$ (also called the 'period') of the orbit segment $\mathbf{x}$ appears as an explicit parameter in (8). The function $\mathbf{u}$ is a unique solution of (8), if suitable boundary conditions are imposed at one or both end points $\mathbf{u}(0)$ and $\mathbf{u}(1)$. A suitable boundary condition presents itself by way of the Stable Manifold Theorem [27, 40], which states that the stable manifold of an equilibrium $p$ or periodic orbit $\Gamma$ is tangent to the linearized manifolds of these invariant objects. Below, we discuss the specific boundary conditions used for computing large, representative parts of the two-dimensional manifolds $W^s(p)$ and $W^s(\Gamma)$, as well as their intersection curves with a plane and sphere, respectively.

### The stable manifold of an equilibrium

A part of interest of the stable manifold $W^s(p)$ of an equilibrium $p$ can be computed as, and represented numerically by, a collection of orbit segments with end points in the linear stable eigenspace $E^s(p)$, at a sufficiently small distance from $p$. If the stable eigenvalues of the linearization at $p$ are real then one requires these end points to lie on a small circle or ellipse in $E^s(p)$ around $p$. When the stable eigenvalues are complex conjugate, as is the case for the saddle-focus $p$ considered in this paper, one requires the end points of orbit segments to lie on an interval

$$\mathbf{u}(1) = \mathbf{w}_0^s + \delta\,(\mathbf{w}_1^s - \mathbf{w}_0^s). \qquad \delta \in [0,1). \tag{9}$$

The two points $\mathbf{w}_0^s, \mathbf{w}_1^s \in \mathbb{R}^3$ are chosen as follows. We consider $\mathbf{w}_0^s = p + \epsilon\,\mathbf{v}^s$, where $\mathbf{v}^s \in E^s(p)$ is a unit (generalized) stable eigenvector of $p$ and $\epsilon > 0$ is small and fixed (we used $\epsilon = 10^{-5}$ throughout). Then $\mathbf{w}_1^s$ is defined as the first return (in backward time) of the orbit through $\mathbf{w}_0^s$ to the local section spanned by $\mathbf{v}^s$ and the unstable eigenvector $\mathbf{v}^u$ of $p$. Hence, the line segment defined in (9) is an approximate fundamental domain, meaning that $\delta \in [0,1)$ uniquely parameterizes the family of orbits on $W^s(p)$; moreover, this line segment lies in an $O(\epsilon^2)$ neighborhood of $W^s(p)$.

The BVP (8)–(9) defines a $(\delta, T)$-dependent family of orbit segments. For any fixed $T = T_0$ we have a uniquely defined one-parameter family of orbit segments that constitutes an accurate approximation of the corresponding part of $W^s(p)$. In order to compute this $\delta$-family by continuation in Auto, we need to specify a first orbit segment that satisfies (8)–(9) for some fixed $\delta = \delta_0 \in [0,1)$. To this end, one considers the trivial orbit segment $\mathbf{u} \equiv \mathbf{w}_0^s$ with $T = 0$; continuation in $T$ for fixed $\mathbf{u}(1) = \mathbf{w}_0^s$ up to $T = -T_0$ yields the desired orbit segment satisfying (8)–(9) for $\delta = \delta_0$. (Note that this continuation step is effectively integration from $\mathbf{w}_0^s$ backward in time.) A continuation in $\delta$ over the interval $[0,1)$ results in a collection of orbits segments, which is then used to render $W^s(p)$ as a surface.

#### Intersections of the manifold with a chosen codimension-one submanifold

Instead of keeping $T$ fixed to perform the continuation, one can choose to restrict the point $\mathbf{u}(0)$. This allows one, for instance, to calculate the intersection set $W^s(p) \cap M$ with a codimension-one submanifold $M = \{\mathbf{x} \in \mathbb{R}^3 : G(\mathbf{x}) = 0\}$, by imposing the second boundary condition

$$G(\mathbf{u}(0)) = 0. \tag{10}$$

Solutions of the BVP (8)–(10) are, hence, orbit segments that start on $M$ and end in the (approximate) fundamental domain of $W^s(p)$ near $p$. For every fixed $\delta$ this BVP has a locally unique solution with a given value of the integration time $T$, which is now a free parameter. This means that we again obtain a one-parameter family of orbit segments, whose begin points $\mathbf{u}(0)$ trace out a curve in $W^s(p) \cap M$. A first orbit segment that satisfies the BVP (8)–(10) can be found by continuation in $T$ of any orbit segment that satisfies (9) for some choice of $\delta \in [0,1)$; we monitor the value of $G(\mathbf{u}(0)$ and stop the continuation when condition (10) is satisfied. Note that not all points on the line segment (9) may reach the submanifold $M$; on the other hand, there may be many disjoint curves in $W^s(p) \cap M$, in which case it is necessary to generate many initial orbit segments that satisfy BVP (8)–(10). Hence, in general, a number of different values of $\delta_0$ need to be chosen to generate suitable first orbits segments. Any such first orbit segment can then be continued as a one-parameter family of solutions of BVP (8)–(10) where $\delta$ and $T$ are free parameters; we refer to [1, 36] for more details

The explicit form of the function $G(\cdot)$ for computing the intersection curves with the plane $\Sigma$ from Section 3.1 is

$$G(\mathbf{x}) = (\mathbf{v}^u \times \mathbf{v}^s) \cdot (\mathbf{x} - p),$$

where $\mathbf{v}^u$ and $\mathbf{v}^s$ are the unstable and stable eigenvectors as above. For the sphere $S_R$ of radius $R$ centered at $p$, as in Section 3.2 and Section 4.1, we consider

$$G(\mathbf{x}) = ||\mathbf{x} - p|| - R. \tag{11}$$

**The stable manifold of a periodic orbit**

The stable manifold $W^s(\Gamma)$ of a periodic orbit $\Gamma$ of saddle type can be computed effectively with the same BVP setup as $W^s(p)$. At each point $\mathbf{q} \in \Gamma$ there is a well-defined stable linear eigendirection spanned by the unit vector $\mathbf{v}^s(\mathbf{q})$ corresponding to the eigenvalue of the Poincaré map at $\mathbf{q}$ with modulus less than 1; this vector family $\{\mathbf{v}^s(q)\ ;\ \mathbf{q} \in \Gamma\}$ forms the stable eigenbundle $E^s(\Gamma)$ of $\Gamma$. By extending system (8) in Auto, one can obtain a discretized version of $E^s(\Gamma)$; see [19, 38] for details.

Once $\mathbf{v}^s(\mathbf{q})$ has been calculated for some fixed choice $\mathbf{q} \in \Gamma$, we choose $\mathbf{w}_0^s = \mathbf{q} + \epsilon\, \mathbf{v}^s(q)$, where $\epsilon$ is again small and fixed, and define $\mathbf{w}_1^s$ to be the first return (in backward time) of the trajectory through $\mathbf{w}_0^s$ to a local planar section that contains $\mathbf{v}^s(q)$; we used the plane with normal $(-v_2, v_1, 0)$, where $\mathbf{v}^s(\mathbf{q}) = (v_1, v_2, v_3)$. A piece of interest of $W^s(\Gamma)$ can now be computed as the $\delta$-family of solution of the BVP (8)–(9) for a fixed choice of $T = T_0$. To obtain intersection curves of $W^s(\Gamma)$ with the sphere $S_R$, we continue the BVP (8)–(10), with $G(\cdot)$ as given by (11). Starting orbits for the continuation are again found by continuation in $T$ in the same way as for $W^s(p)$.

We remark that attention must be paid to the orientation of $W^s(\Gamma)$. If the Floquet multipliers are both positive, then $W^s(\Gamma)$ is an orientable surface, that is, it consists of two half-cylinders that are joined smoothly at $\Gamma$. Hence, $W^s(\Gamma)$ has two sides that need to be computed separately; this can be achieved by considering both $+\mathbf{v}^s(\mathbf{q})$ and $-\mathbf{v}^s(\mathbf{q})$ in the definition of $\mathbf{w}_0^s$. If $\Gamma$ has two negative Floquet multipliers, on the other hand, then its stable manifold is a non-orientable surface, that is, a Möbius strip locally near $\Gamma$. In particular, this means that changing the parameter $\delta$ in (9) over the interval $[0, 1)$ yields the respective piece of $W^s(\Gamma)$ in a single continuation. We refer to [47] for more details about non-orientable manifolds.

The BVP approach used in this paper provides efficient and accurate approximations of global invariant manifolds; see [15, 36] for more examples. The high accuracy of our computations is evidenced, in particular, by the images of the sets $W^s(p) \cap S_R$, $W^s(\Gamma_{\mathbf{A}}) \cap S_R$, $W^s(\Gamma_{\mathbf{B}}) \cap S_R$, and $W^s(\Gamma_{\mathbf{C}}) \cap S_R$ in Figs. 18 and 19. Despite the fact that these four interleaved sets of curves were obtained in separate continuation runs and with different boundary conditions, they align perfectly without intersecting each other. Furthermore, thanks to the BVP formulation, we are able to identify each intersection curve in the figures of Sections 3 and 4 in one-to-one correspondence with a specific subinterval of the associated fundamental domain. This ensures, in particular, that no curve is repeated in the figures.